BULLETIN OF MATERIALS SCIENCE AND METALLURGY

Volume 2 I Issue 1 I Pages 1-27 I 2025

ONLINE ISSN:3023-6509

bulletinofmsm.org/

BULLETIN OF MATERIALS SCIENCE AND METALLURGY

BULLETIN OF MATERIALS SCIENCE AND METALLURGY

BULLETIN OF MATERIALS SCIENCE AND METALLURGY

BULLETIN OF
MATERIALS SCIENCE AND METALLURGY

CONTENTS

Bulletin of Materials Science & Metallurgy

Periodical Scientific Journal of UCTEA Chamber of Metallurgical and Materials Engineers

Volume 2, Issue 1, 2025, Pages 1-5 Received: 21 October 2024 Accepted: 18 October 2025
https://doi.org/10.70342/YCIN5024

Review Article

The Importance of Green Transport Today: Time for Hydrogen Buses

Songül KILINÇ[a,*], Ferhat AĞAÇ[a], Nurşah Kübra EKMEKÇİ[a] and Samet Onur EMİR[a]

[a] Güleryüz Bus Company R&D Center, Bursa

*Corresponding author's email: songul.kilinc@guleryuz.com

Abstract

New technologies are being developed to reduce CO_2 emissions due to climate change and increasingly stringent sustainability standards, which are prominent both globally and nationally. In response, the automotive sector has begun transitioning from diesel buses to electric buses (E-buses), and more recently to hydrogen-powered buses (H-buses). Many public transport companies have already completed pilot projects involving hydrogen fuel cell buses (FCEBs), signaling growing confidence in this emerging technology. This paper aims to present the technical, environmental, and economic prospects of hydrogen fuel cell buses. It investigates the necessary steps and potential challenges in achieving carbon neutrality within the competitive bus transportation market. Expectations and obstacles related to fuel cell vehicles have been identified. As the use of renewable energy becomes better integrated into buses, interest in this area has grown. A key advantage is their lower CO_2 emissions compared to diesel buses. Although the technology may seem immature, hydrogen buses are expected to reduce CO_2 emissions by 93% compared to diesel buses. Despite their environmental benefits, hydrogen buses face economic challenges. Notably, their initial investment cost is approximately 40% higher than that of diesel buses. However, ongoing technological advancements and increased R&D efforts are expected to reduce this cost disparity over time. With the right policy support and infrastructure investment, hydrogen buses have strong potential to play a leading role in the decarbonization of public transportation.

Keywords

CO_2 emission, Energy efficiency, Green transport, Hydrogen bus, Sustainability

1. Introduction

In urban settings, private car usage is a major contributor to overall carbon emissions, while public transport is widely regarded as a more environmentally sustainable mode of travel. Developed countries have long made significant improvements in improving air quality in densely populated cities. They advocate for the use of alternative energy sources in transportation as a way to reduce air pollution, particularly emphasizing the use of electric buses powered by hydrogen fuel cells as a significant factor in achieving air quality and pollution reduction goals [1].

With the Paris Agreement, the goal is set to keep global warming below 2°C above pre-industrial levels and to pursue efforts to limit the temperature increase to 1.5°C above pre-industrial levels within this century. Furthermore, to achieve these goals, it is desired that greenhouse gas emissions reach optimum levels and decrease as rapidly as possible [2]. Considering the conditions of the Paris Agreement, fuel cell electric buses (FCEBs) are anticipated to offer numerous operational, environmental, and economic benefits compared to traditional diesel or diesel hybrid buses. These buses operate with significant reductions in greenhouse gas emissions, without any local emissions, less noise, and with performance, range, and route flexibility [3].

As part of its commitment to the goals of the Paris Agreement, the United Kingdom believed that more emphasis should be placed on decarbonizing public transportation and moving away from conventional fuel vehicles (CFVs) and electric vehicles (EVs) in personal transportation. They were of the opinion that electric buses (EBs) and hydrogen buses (HBs), powered by low-carbon renewable energy sources, have the potential to meet all requirements. A comparison of carbon dioxide (CO_2) emissions produced by conventional fuel buses (CFBs), EBs, and HBs between 2017 and 2050 was conducted. Emissions per person for CFBs, HBs, EBs, and personal transportation at different vehicle capacity levels (100%, 75%, 50%, and 25%) were estimated assuming a maximum of 80 passengers per bus and four passengers per personal vehicle. The results indicated that by 2050, conventional fuel buses would produce 16.3 gCO_2 km-1 per person compared to 30 gCO_2 km-1 per person for conventional fuel vehicles. Considering all these scenarios, at 100% capacity, it was concluded that by 2050, emissions from conventional fuel buses would be 36 times higher than electric buses, 9 times higher than hydrogen buses, and 12 times higher than electric vehicles. Cumulative emissions under all electric scenarios remained lower for EBs and HBs by 2050 [4].

Electric buses are powered by a lithium-ion battery charged with electricity [5]. However, if the electricity is generated from fossil fuels, the environmental benefits will be reduced [6, 7]. Hydrogen buses, on the other hand, are powered by fuel cells that convert hydrogen (H_2) into electricity and emit water vapor as a byproduct [5]. H_2 is chemically produced by splitting water into oxygen and H_2 using electricity or by converting carbon monoxide with methane into H_2, as a byproduct. Additionally, using H_2 as a fuel for buses with fuel cell propulsion systems will provide an opportunity for a sustainable alternative by allowing the replacement of mineral oils [8]. The transition to an H_2 energy system will likely rely on electrolysis supported by the National Grid, which may involve a mixture including H_2 derived from natural gas or fossil fuel-powered plants. Similar to EBs, it is believed that if H_2 is produced from fossil fuels, there will be no advantage in transitioning from conventional fuel buses unless carbon emissions can be indefinitely isolated as an inert chemical or in a geological repository [1]. Comparison of the properties of hydrogen and diesel fuel is given in Table 1. In Figure 1, the types of fuel used are classified according to vehicle types.

Table 1. Properties of hydrogen and diesel fuel [9].

Property	**Diesel Fuel**	**Hydrogen**
Moleculer weight, [kg/kmol]	226	2.016
Density at 0°C, 760 mmHg, [kg/m³]	820-860	0.0899
Ignition limits in air, at 20°C, 760 mmHg, % vol	0.7-5	4.1-75.6
Ignition limits in air, at 20°C, 760 mmHg, Λi..λs	0.34..1.68	0.136..10.12
Heat of vaporization [kJ/kg]	250-314	458.1
Boiling temperature, °C, la 101300 Pa	180-359	-253
Diffusivity in air, cm²/s	0.038	0.63
Energy Density at 15°C, 100kPa, MJ/m³	35.8	10.3

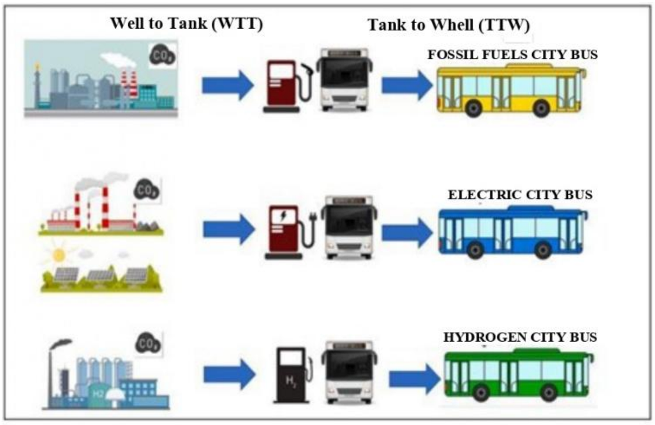

Figure 1. Fuel types used according to vehicle types [10].

For any new technology to enter the market and be used, acceptance is crucial. Failure in marketing and acceptance of the product can lead to inadequate adoption of the technology or even resistance or opposition to it [11]. Among experts in hydrogen technology, the widespread perception that the public may reject new H_2 technologies due to associations with the 1937 Hindenburg disaster or 'hydrogen' bomb has been considered [12, 13]. The importance of determining the acceptability of hydrogen-fueled transportation by the public and engaging the public in discussions about the future of hydrogen transportation has been addressed and debated with numerous documents [14, 15]. Hydrogen (H_2) buses are being tested in selected cities worldwide, providing practical experience in their operation, maintenance, and the development and operation of relevant H_2 fueling infrastructure [16].

While public transportation is generally cleaner and cheaper than driving cars, there are compelling factors to consider in the choice, especially in large cities like those in South America. Despite the low costs of internal combustion engine vehicles, the high acquisition cost of zero-emission vehicles slows down the entry of electric vehicles and fuel cell hydrogen vehicles into the market. This situation is even more pronounced in South America, where the entry of electric vehicles into the market is very low. In 2018, there were 250 electric vehicles and 680 plug-in hybrid electric vehicles in stock in Chile and Brazil, representing less than 0.03% of the global stock of 3 million [17].

2. Evaluation of Hydrogen

Hydrogen vehicles represent a promising advancement in the quest for sustainable and environmentally friendly transportation solutions. Unlike conventional gasoline-powered cars, hydrogen vehicles utilize a fuel cell to convert hydrogen gas into electricity, emitting only water vapor as a byproduct. This innovative technology offers the potential for zero-emission driving while providing the convenience of quick refueling and extended driving ranges. As the world increasingly shifts towards reducing carbon footprints and combating climate change, hydrogen vehicles emerge as a viable and attractive option for the future of mobility. However, several challenges remain before full cell electric vehicles can achieve widespread adoption. The primary issue is the limited hydrogen refueling infrastructure, with only a few stations available in India, restricting the range and usability of these vehicles. Additionally, hydrogen production and storage costs are currently higher than traditional fuels, though this is expected to improve as the technology advances [18].

Components required for a hydrogen vehicle;

Hydrogen Storage Tank: It safely contains the hydrogen fuel until it is needed for energy conversion in the fuel cell.

Fuel Filler: The nozzle from a fuel dispenser connects to the vehicle's receptacle to fill the tank

Fuel Cell Stack: The core component where hydrogen reacts with oxygen to produce electricity.

Battery(auxiliary): In an electric vehicle, the low-voltage auxiliary battery starts the car and powers accessories before the traction battery engages

Battery Pack: It stores excess energy generated by the fuel cell and regenerative braking, providing additional power during high demand situations like acceleration.

Electric Motor: It converts electrical energy from the fuel cell and battery into mechanical energy to propel the vehicle.

Power Control Unit (PCU): It regulates the flow of electricity between the fuel cell, battery, and electric motor to ensure efficient operation.

Air Compressor: It ensures an adequate supply of oxygen to the fuel cell for the electrochemical reaction with hydrogen.

Cooling System: It manages the temperature of the fuel cell stack and other components to prevent overheating and maintain optimal performance.

Hydrogen Sensors: They detect any hydrogen leaks and alert the driver or initiate safety protocols to prevent accidents.

Regenerative Braking System: It converts kinetic energy back into electrical energy, which is then stored in the battery for later use.

Vehicle Control Unit (VCU); It coordinates the operation of all components, ensuring the vehicle operates efficiently and safely.

Inverters: They ensure the electric motor receives the correct type of electrical current to operate.

Within the fuel cell (FC) industry, five key market segments have been identified: portable, stationary, vehicle propulsion, fuel infrastructure, and auxiliary power units. Portable applications account for more than 50% of the market share, whereas stationary applications represent around 20%. Between 2003 and 2006, there was a 26% increase in R&D expenditures and a 36% increase in the number of workers across companies working on this subject. Between 2005 and 2008, there was a 4-fold increase in portable units. Large companies have produced or are in the R&D of different types of portable fuel cells, especially for military use, and are awaiting commercialization [19].

3. FCEVs vs BEVs

Hydrogen fuel cell vehicles (FCEVs) and battery electric vehicles (BEVs) each have their own set of advantages and disadvantages, depending on technological characteristics and infrastructure requirements. One of the main advantages of hydrogen vehicles is their shorter refueling time. Unlike electric vehicles that can take several hours to fully recharge, hydrogen vehicles can be refueled in just 3-5 minutes, similar to conventional gasoline vehicles. This makes them more convenient for long trips and commercial applications where downtime needs to be minimized [20].

FCEVs (Fuel Cell Electric Vehicles) operate similarly to BEVs but on hydrogen. A fuel cell is used for this. The vehicle has a special tank to hold pressurized hydrogen. The hydrogen is then passed through a fuel cell; It produces electricity by combining hydrogen and oxygen from the air using electrolysis to produce only H_2O as a byproduct, which charges a small capacity battery [21]. FCEVs have a clear advantage over other battery-powered vehicles as they do not need to be charged and can be charged in just a fraction of the time. The average fuel cell electric car can travel between 400 and 500 carbon-free miles.

However, hydrogen vehicles also face several challenges. The production, storage, and distribution infrastructure for hydrogen is currently underdeveloped and costly to build. In contrast, the infrastructure for charging electric vehicles is more widespread and continually expanding. Producing hydrogen, especially green hydrogen, is energy-intensive and expensive, making the overall cost of hydrogen vehicles higher. In terms of energy efficiency, hydrogen vehicles are generally less efficient than electric vehicles because of the energy losses that occur during hydrogen production, storage, and conversion back to electricity in the fuel cell. FCEVs weigh more than BEVs because they have 1-2 tanks and multiple fuel cells, which reduces the practicality of the vehicle [22]. Many automobile companies have begun to invest in hydrogen as an alternative fuel. However, production has been suspended due to the high cost of producing carbon-free hydrogen and transporting high-pressure hydrogen to fuel facilities [23].

Moreover, the technical challenges associated with hydrogen storage and transport are significant. Hydrogen needs to be stored at high pressures or at very low temperatures, both of which require advanced and expensive technology to ensure safety and efficiency. Despite these challenges, hydrogen vehicles hold great potential for reducing dependence on fossil fuels and lowering greenhouse gas emissions, especially in applications where electric vehicles might not be as practical.

4. Test standards for Hydrogen Buses

For hydrogen fueled vehicles, basic tests as well as ECE R134 Safety-related performance of hydrogen fuelled vehicles and 2021/535 Annex XIV - Hydrogen System Material Compatibility and Fuelling Receptacle regulations must be approved.

To give an example of a requirement also mentioned in the ECE R134 Regulation, all new compressed hydrogen storage systems for road vehicles must have a nominal working pressure of 70 MPa or less and a service life of 15 years or less [24].

Also as mentioned in the ECE R134 Regulation, The hydrogen storage system shall meet the performance test requirements specified in this paragraph. The qualification requirements for on-road service are:

-Verification tests for baseline metrics,

-Verification test for performance durability (hydraulic sequential tests),

-Verification test for expected on-road system performance (pneumatic sequential tests),

-Verification test for service terminating system performance in fire,

-Verification test for performance durability of primary closures [25].

To mention some of the obligations that must be made according to the 2021/535 Annex XIV regulation, in the case of hydrogen vehicles of M3, labels shall be installed on the front and rear of the vehicle, in the vicinity of the fueling receptacle and to the side of each door or set of doors [25].

5. Conclusion

Considering the type of fuel, hydrogen bus technology replaces new generation technologies with its environmental friendliness and low emissions. However, as can be understood from R&D studies, it has advantages and disadvantages compared to other electric and diesel vehicles.

Hydrogen vehicles also generally offer a longer driving range compared to many electric vehicles. It can generally travel 500-700 kilometers with a single hydrogen tank, which is especially advantageous in long-distance driving. Additionally, hydrogen fuel cells perform better in cold weather conditions compared to batteries, which will result in a loss of efficiency at low temperatures. This makes hydrogen vehicles a more reliable option in colder climates.

Another important advantage is its suitability for heavy-duty applications. Hydrogen vehicles are well-suited for heavy transport vehicles such as trucks, buses and other commercial vehicles due to their high energy density and rapid refueling capabilities. This has made them a promising option for industries requiring long-distance and heavy load transportation. High costs stand out as the biggest disadvantage in the production sector.

Authors' Contributions

Methodology: Songül Kılınç; Ferhat Ağaç; Nurşah Kübra Ekmekçi; Samet Onur Emir, Investigation: Songül Kılınç; Ferhat Ağaç; Nurşah Kübra Ekmekçi; Samet Onur Emir, Data curation: Songül Kılınç, Writing – original draft: Songül Kılınç, Writing – review and editing: Songül Kılınç, Project administration: Songül Kılınç

References

[1] Hua, T., Ahluwalia, R., Eudy, L., Singer, G., Jermer, B., Asselin-Miller, N., ... & Marcinkoski, J. (2014). Status of hydrogen fuel cell electric buses worldwide. *Journal of Power Sources*, *269*, 975-993.

[2] Pietzcker, R. C., Longden, T., Chen, W., Fu, S., Kriegler, E., Kyle, P., & Luderer, G. (2014). Long-term transport energy demand and climate policy: Alternative visions on transport decarbonization in energy-economy models. *Energy*, *64*, 95-108.

[3] Grüger, F., Dylewski, L., Robinius, M., & Stolten, D. (2018). Carsharing with fuel cell vehicles: Sizing hydrogen refueling stations based on refueling behavior. *Applied energy*, *228*, 1540-1549.

[4] Logan, K. G., Nelson, J. D., & Hastings, A. (2020). Electric and hydrogen buses: Shifting from conventionally fuelled cars in the UK. *Transportation Research Part D: Transport and Environment*, *85*, 102350.

[5] Charters, D. (2016). A comparison of energy vectors in powering hybrid buses. *Renewable Energy Focus*, *17*(2), 73-74.

[6] Correa, G., Muñoz, P., Falaguerra, T., & Rodriguez, C. R. (2017). Performance comparison of conventional, hybrid, hydrogen and electric urban buses using well to wheel analysis. *Energy*, *141*, 537-549.

[7] Mekhilef, S., Saidur, R., & Safari, A. (2012). Comparative study of different fuel cell technologies. *Renewable and Sustainable Energy Reviews*, *16*(1), 981-989.

[8] Emonts, B., Schiebahn, S., Görner, K., Lindenberger, D., Markewitz, P., Merten, F., & Stolten, D. (2017). Re-energizing energy supply: Electrolytically-produced hydrogen as a flexible energy storage medium and fuel for road transport. *Journal of Power Sources*, *342*, 320-326.

[9] Popa, M. G., Negurescu, N., & Pana, C. (2003). Diesel Engines. Processes. *Matrix*, *1*(2), 1-703.

[10] Hensher, D. A., Wei, E., & Balbontin, C. (2022). Comparative assessment of zero emission electric and hydrogen buses in Australia. *Transportation Research Part D: Transport and Environment*, *102*, 103130.

[11] Bauer, M. W. (1995). *Resistance to new technology: nuclear power, information technology and biotechnology*. Cambridge university press, pp. 1-42. https://doi.org/10.1017/CBO9780511563706.002

[12] Foley, J. (2001). H2: driving the future. *IPPR: London, UK*, p50.

[13] Adamson, K. A., & Pearson, P. (2000). Hydrogen and methanol: a comparison of safety, economics, efficiencies and emissions. *Journal of power sources*, *86*(1-2), 548-555.

[14] Midden, C, Montijn-Dorgelo, F., 2004. Developing and introducing hydrogen technology, an analysis of social psychological factors-paper written for NOW programme CW/ACTS, Eindhoven.

[15] Schulte, I., Hart, D., & Van der Vorst, R. (2004). Issues affecting the acceptance of hydrogen fuel. *International Journal of Hydrogen Energy*, *29*(7), 677-685.

[16] O'Garra, T., Mourato, S., Garrity, L., Schmidt, P., Beerenwinkel, A., Altmann, M., ... & Whitehouse, S. (2007). Is the public willing to pay for hydrogen buses? A comparative study of preferences in four cities. Energy Policy, 35(7), 3630-3642.

[17] Correa, G., Muñoz, P. M., & Rodriguez, C. R. (2019). A comparative energy and environmental analysis of a diesel, hybrid, hydrogen and electric urban bus. *Energy*, *187*, 115906.

[18] Chandran, M., Palanisamy, K., Benson, D., & Sundaram, S. (2022). A review on electric and fuel cell vehicle anatomy, technology evolution and policy drivers towards EVs and FCEVs market propagation. *The Chemical Record*, *22*(2), e202100235.

[19] Suominen, A., & Tuominen, A. (2010). Analyzing the Direct Methanol Fuel Cell technology in portable applications by a historical and bibliometric analysis. *Journal of Business Chemistry*, *7*(3).

[20] Sanguesa, J. A., Torres-Sanz, V., Garrido, P., Martinez, F. J., & Marquez-Barja, J. M. (2021). A review on electric vehicles: Technologies and challenges. Smart Cities, 4(1), 372-404.

[21] Tarroja, B., Zhang, L., Wifvat, V., Shaffer, B., & Samuelsen, S. (2016). Assessing the stationary energy storage equivalency of vehicle-to-grid charging battery electric vehicles. Energy, 106, 673-690.

[22] Gondal, I. A., Masood, S. A., & Khan, R. (2018). Green hydrogen production potential for developing a hydrogen economy in Pakistan. International Journal of Hydrogen Energy, 43(12), 6011-6039.

[23] Manoharan, Y., Hosseini, S. E., Butler, B., Alzhahrani, H., Senior, B. T. F., Ashuri, T., & Krohn, J. (2019). Hydrogen fuel cell vehicles; current status and future prospect. Applied Sciences, 9(11), 2296.

[24] <https://unece.org/fileadmin/DAM/trans/main/wp29/wp29regs/2015/R134e.pdf> Dated:15.05.2024

[25] <https://eur-lex.europa.eu/legal-content/EN/TXT/PDF/?uri=CELEX:32021R0535&qid=1716798750562> Dated: 15.05.2024

BMSM

Bulletin of Materials Science & Metallurgy

Periodical Scientific Journal of UCTEA Chamber of Metallurgical and Materials Engineers

Volume 2, Issue 2, 2025, Pages 6-13 Received: 11 April 2025 Accepted: 08 October 2025
https://doi.org/10.70342/EFHM8547

Research Article

Investigation of Sintering Temperature Effect on Scandate Cathode Pore Structure and Mathematical Expression

Zeynep Hazal Yazğan[a,*], Nergis Yıldız Angın Atmaca[b] and Okan Mert Yücedağ[c]

[a]Department of Metallurgical and Materials Engineering, Istanbul Technical University, Istanbul, Türkiye
[b]TÜBİTAK BİLGEM, Kocaeli, Türkiye
[c]RST Technology, Türkiye

*Corresponding author's email: yazgan25@itu.edu.tr

Abstract

In this study, changes in the surface pore structure depending on the sintering temperature of the cathodes used in vacuum electronic devices were investigated. Ammonium meta tungstate (AMT) $[(NH_4)_6(H_2W_{12}O_{40})_4H_2O]$(99.9% w/w), $Sc(NO_3)_3$(99.99% w/w), and 4:1:1 barium calcium aluminate (BCA) were purchased and used without further purification. Tungsten powders were doped with scandium nitrate and BCA. After synthesizing the powder, consecutive material characterization analyses were conducted. The sintering processes were carried out at different temperatures in a hydrogen atmosphere and the pore structure was studied in detail by SEM and EDS analyses.

The experimental data were analysed with a mathematical modelling to investigate the relationship between sintering temperature and pore diameters. Two pieces of function were utilized to describe the pore size and sintering temperature relation. The effect of sintering temperature on the pore structures of the cathode surface has been studied and the importance of pore dimensions on cathode performance and life has been emphasized. Therefore, this mathematical modelling offers a promising prediction technique by saving time and cost.

Keywords

scandate cathode, sintering, pore structure, mathematical modelling

1. Introduction

In vacuum electronic devices, cathodes are used as an electron source which is required for electron beam energy supply to the system [1]. So, there are some basic needs for dispenser cathodes such as high current density and long lifetime [2]. To meet these needs, scandate thermionic cathodes have been attracting great attention for decades [3]. They exhibit most up-to-date properties among the other dispenser cathode species in terms of higher current density, lower operating temperature and longer life [4]. However, when the current density of the cathodes is higher, the emission performance of the cathode deteriorates due to the gases released. Therefore, it is crucial for a cathode to have ion bombardment resistant pore structures [5]. Thus, the surface characteristics of scandate pellets should be analysed in detail.

Tungsten is generally used as a fundamental matrix material for cathodes and powder metallurgical techniques are used for fabrication of cathodes in most cases [6]. Powder particle shape, dimension, purity, sintering parameters and pore characteristics of the sintered pellet directly affect the performance of cathodes. In this study, all of the scandate cathode fabrication materials were prepared in spray dryer device so as to collect homogeneous powders. In literature, there are various kind of scandate cathode production types. The main focus is based on fabrication of these types of cathodes such as traditional impregnated scandate cathodes, top layer cathodes, impregnated mix matrix scandate cathodes, pressed scandate cathodes and spray dried scandate cathodes [7]. The majority of works in this field is experimental. There is a lack of studies in the literature that incorporate computational inductive methodologies based on experimental data. This is exactly the point at which the novel aspect of our study becomes significant. In this study, both the most advanced manufacturing technology was employed and a model was developed to establish the relationship between sintering temperature and cathode pore size based on experimental data. To the best of our knowledge, there is no study in the literature that uses experimental sintering temperature data to investigate the relationship with pore size.

Characterization studies including X-Ray Diffractometer (XRD), Scanning Electron Microscope (SEM), Energy Dispersive Spectrometer (EDS) were performed. After getting proper chemical forms and amounts, cold isostatic pressing and sintering studies were conducted. The pellets were sintered at different temperatures to observe the temperature effects on the pore structures. Surface porosity, shrinkage values and pore sizes were analysed and calculated. Pore size values were correlated with sintering temperatures. Finally, it was obtained a mathematical relation that explains the sintering behaviour of pellets and pore size alteration with temperature. Thus, one can easily estimate the pore sizes before sintering procedure in advance.

2. Materials and Methods

2.1. Preparation of co-doped tungsten (CDT) powder

Commercial AMT $[(NH_4)_6(H_2W_{12}O_{40})_4H_2O]$ (99.9% w/w), scandium nitrate ($Sc(NO_3)_3$) (99.99% w/w), and 4:1:1 BCA were used as raw materials. CDT powders were prepared by dissolving AMT, $Sc(NO_3)_3$, and BCA in water followed by spray drying method with combined calcination and hydrogen reduction processes. The solution which is composed of AMT, $Sc(NO_3)_3$ and BCA was mixed and a homogeneous powder was obtained. In order to ensure the homogeneity and sphericality of the powder, many experiments were conducted. In the final stage, it can be seen in Figure 1 that we have achieved the desired form.

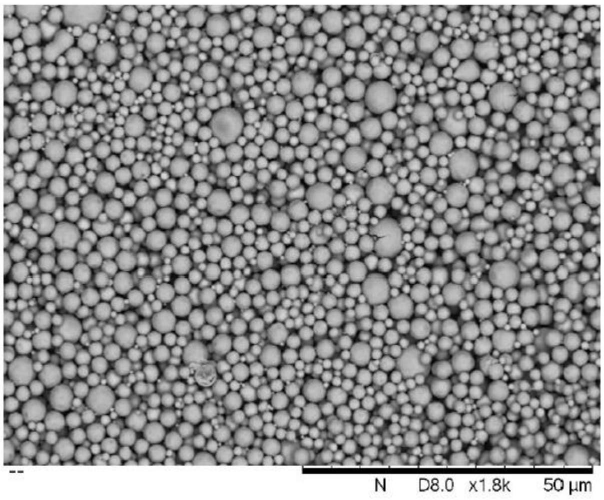

Figure 1. SEM image of spray dried raw powder

In Figure 2, the powder production steps are explained and given below:
1: Scandium nitrate, AMT and BCA water solution which is used in spray drying
2: Raw powder SEM analysis after spray drying
3: Raw powder physical form is calcinated in ceramic furnace
4: Calcinated powder is reduced in hydrogen atmosphere
This procedure is performed sequentially in an iterative manner until getting the aimed homogeneous powder form.

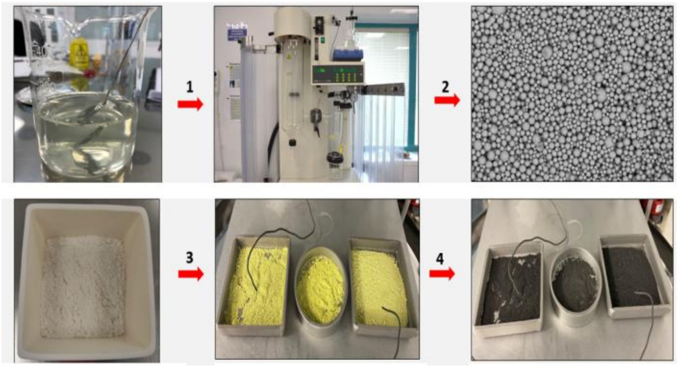

Figure 2. Cathode powder fabricating process steps

2.2. Microstructure characterization and analyses

After obtaining mixed raw powder, consecutive characterization methods were applied in order to identify the properties of powder. Raw powders were subjected to heat treatment to reduce them. Phase identification of reduced CDT (r-CDT) powder was investigated with an XRD, which was carried out using Cu Kα radiation at 40 kV and 20 Ma. The particle size was analysed with a Malvern Instruments MASTERSIZER 2000. SEM-EDS was used to characterize morphology of powders and sintered r-CDT pellet. Pore size measurements of r-CDT pellets were completed, and average pore sizes were calculated from SEM image data sets for each sintering condition by using ImageJ software. Porosity can be calculated as a ratio of the area of pores to the total area of sample analysed [8]. Therefore, SEM images were collected to calculate the porosity % of r-CDT sintered at different temperatures (Equation 1):

$$P\% = \frac{Pores\ Area}{Total\ Area} x100 \quad (1)$$

Conducted experiment data were analysed and modelling studies were conducted.

The powder was spray dried first, then calcined in air atmosphere and finally reduced one more time in hydrogen atmosphere.

At the final stage, scandia doped tungsten powder was obtained. The pellet structures were fabricated with cold isostatically pressing technique. They were prepared for sintering process.

2.3. Sintering Process

r-CDT powders were cold isostatically pressed and then sintered at 1425, 1500, 1575, 1650, 1725, 1800 ºC in the controlled atmosphere. Tungsten is generally sintered at high temperature above 2000 ºC to gain full density. However, there is no need of full density for some cathode applications. Therefore, sintering temperature of tungsten can be reduced to control of the microstructure by alternative techniques [9]. It is explained in literature that, sintering temperature of tungsten is between 1500-2200 ºC to form porous matrix for cathode application [10]. In present study, lower sintering temperature is chosen as 1425 ºC because barium-containing compound ($BaWO_4$ and Ba_2CaWO_6) which formed after reduction, melts temperature above 1400 ºC [11].

In this study, upper limit is chosen as 1800 ºC because extra-high sintering temperature is not preferred to prevent it from melting away. In previous studies, sintering temperature for barium tungsten cathode is preferred 1800-1900 ºC [12].

3. Experimental Results and Discussion

Particle size distribution of doped tungsten powder is given in Figure 3. The powder particle size was measured as approximately 7 µm.

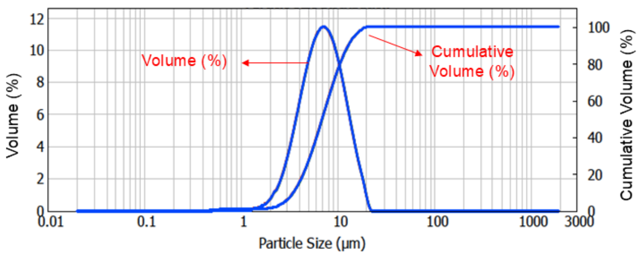

Figure 3. Particle size distribution of doped tungsten powder

The SEM images of processed powder are shown in Figure 4. As it can be seen, the particles maintain their spherical shape. The SEM images show that with the increasing effect of heat treatment on samples, the particle size of samples was progressively decreased.

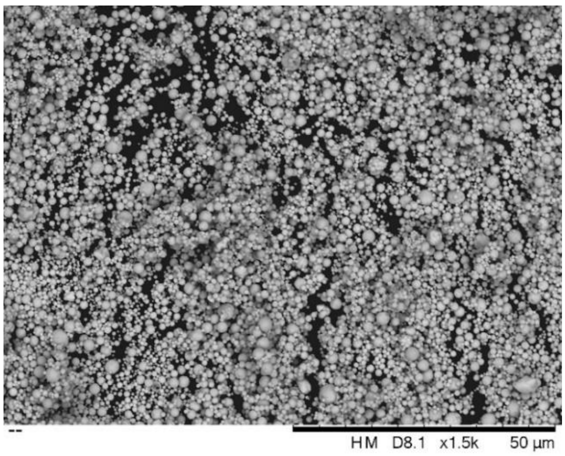

(a)

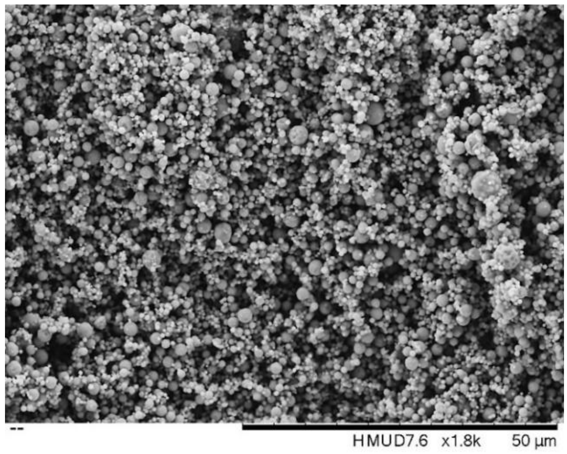

(b)

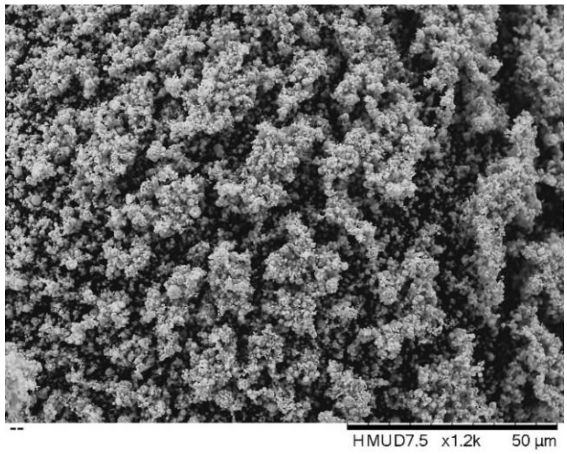

(c)

Figure 4. SEM image of (a) raw powder form after spray drying (b) raw powder after calcination (c) powder after hydrogen reduction

The SEM-EDS analyses of the CDT and r-CDT are given in Figure 5. As shown Figure 5 (a) CDT powder prepared by spray drying have spherical shape without agglomeration. After reduction, r-CDT retained its spherical shape but with agglomeration. It can be seen that particle size of r-CDT is smaller than calcined CDT. On the other hand, it's reported that fine grains form due to pinning effect after reduction [13]. The average size of r-CDT powder particles has been measured to be approximately 6-7 µm, indicating that the material predominantly consists of fine grains. Due to their small size, these fine grains tend to aggregate, as seen in the Figure 5 (c-e). When Figure 5 (e-f) is investigated, scandia is distributed homogenously in both areas. In literature, it is explained that uniform distribution of scandia increases the emission performance of cathodes [13].

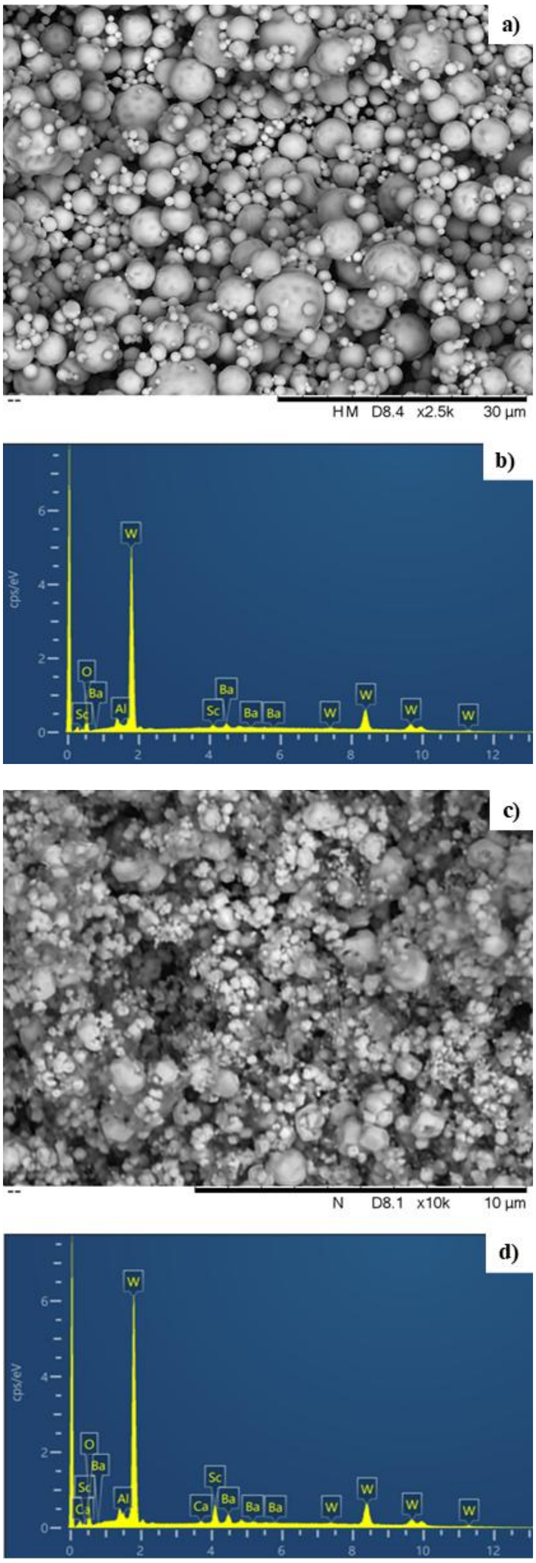

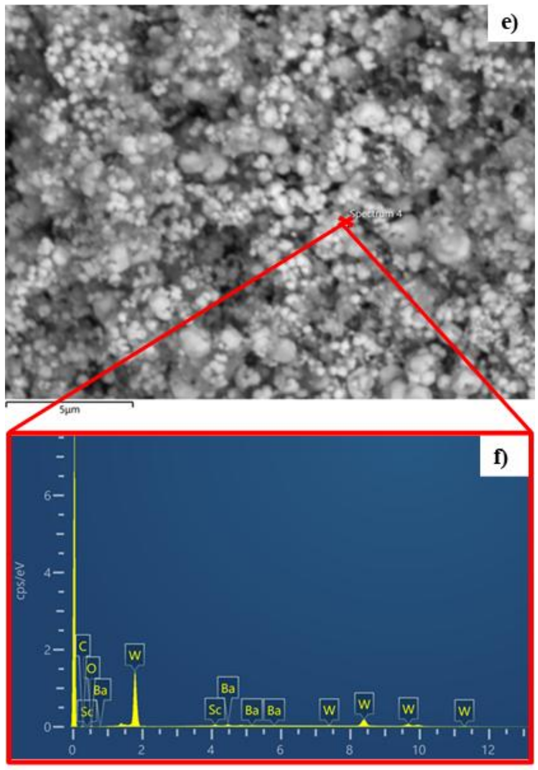

Figure 5. a) SEM and b) EDX of CDT powder, c-e) SEM and d-f) EDX of r-CDT powder

Figure 6 shows XRD pattern of r-CDT. It has been determined that the r-CDT mainly consists of W, Sc_2O_3, $BaWO_4$ and Ba_2CaWO_6 phases (Figure 6). Ba_2CaWO_6 is known as ternary compound in CaO-BaO-WO_3 system. Also, Ba_2CaWO_6 phase reacts with W and transforms into $3(Ba_{1/3}Ca_{2/3})WO_4$ and Ba (Equation 2) [11].

$$2Ba_2CaWO_6 + W \rightarrow 3(Ba_{1/3}Ca_{2/3})WO_4 + Ba \quad (2)$$

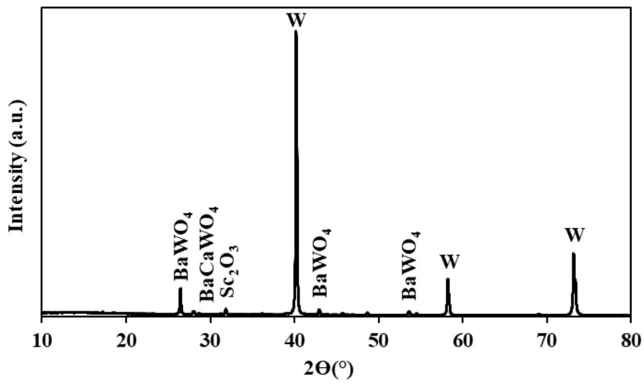

Figure 6. XRD pattern of r-CDT powder

Figure 7 represents that the differences between pellet surfaces. It is apparent that the pores of the pellet structure are interconnected, and sintering has occurred. In addition to sintering, impregnant materials are observed apparently on the surface. Some pores are full of impregnates and some of them are empty. This is a proper structure that can allow free barium to evaporate and flow through the pores during operation.

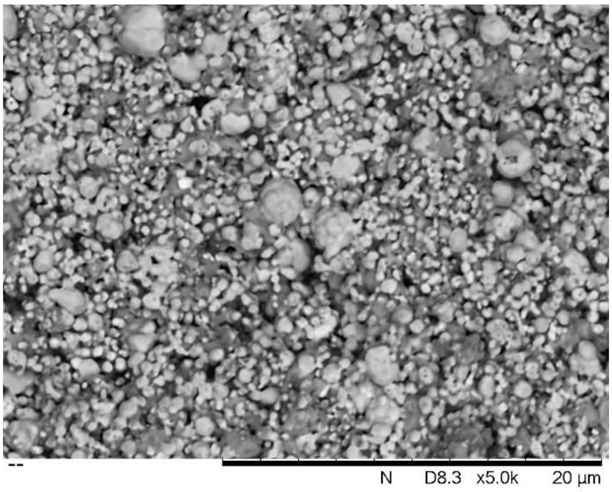

(a)

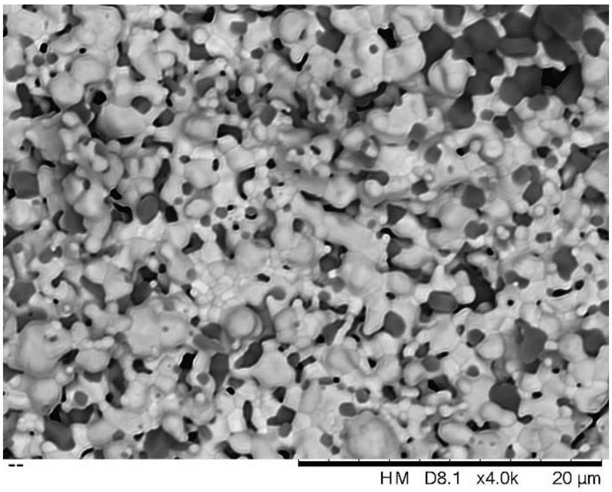

(b)

Figure 7. SEM images of pellets after sintering at (a) 1425 ºC and (b)1800 ºC

Relationship between volume shrinkage and sintering temperature is shown in Figure 8 (a). As the temperature increases, volume shrinkage increased from 4% to 28%. This situation indicates that sintering continues with increasing temperature, and that further temperature increments can contribute to densification. Average pore sizes at different temperature are presented in Figure 8 (b). From 1425 ºC to 1650 ºC, average pore size increased with increasing temperature, while, above 1650 ºC, average pore size decreased. Calculated total porosity according to Equation 1 is shown in Figure 8 (c). As the sintered temperature increases from 1425 ºC to 1500 ºC, porosity remained the same and increased until 1650 ºC. However, after 1650 ºC, it decreased steeply from 11% to 4%. As can be seen on Figure 8 (c) porosity changes as a function of sintering temperature [14]. Pore size distribution shifted towards the higher radius side as increasing temperature from 1425 ºC to 1650 ºC. At 1725 ºC, the pores within 1.2-1.4 µm could not be detected. Therefore, pore size distribution curves shifted towards the left.

Based on the results, sintering process can be classified in three stages according to pore size variation with temperature as shown in Figure 8 (b). So, the first stage is called initial phase in which pore growth is insignificant with temperature change. The second stage is called intermediate phase that pore size increase dramatically until the temperature reaches the sintering value. It is known that pore growth in intermediate stage can be related to particle arrangement occurring by diffusion [15]. As expected, the larger sized pores relative to the initial phase are observed in pore size distribution in Figure 9. However, because of the pores are united with the grain boundaries and eliminated with diffusion in the final stage, a decrease in the pore size may occur [16].

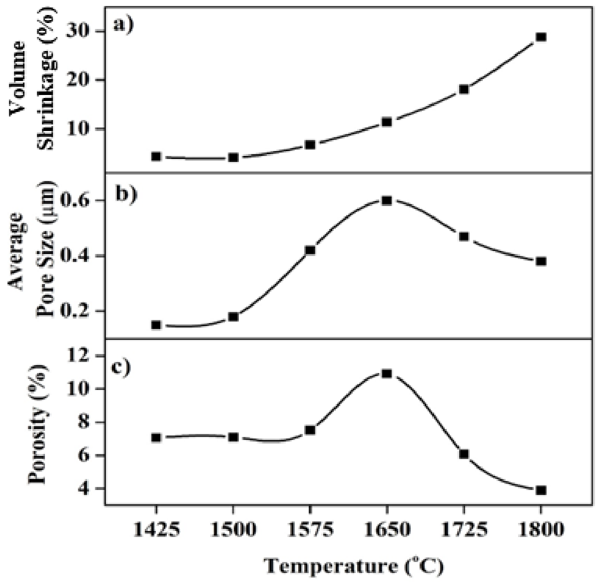

Figure 8. a) Volume shrinkage, b) average pore size and c) porosity of sintered r-CDT at different sintering temperature

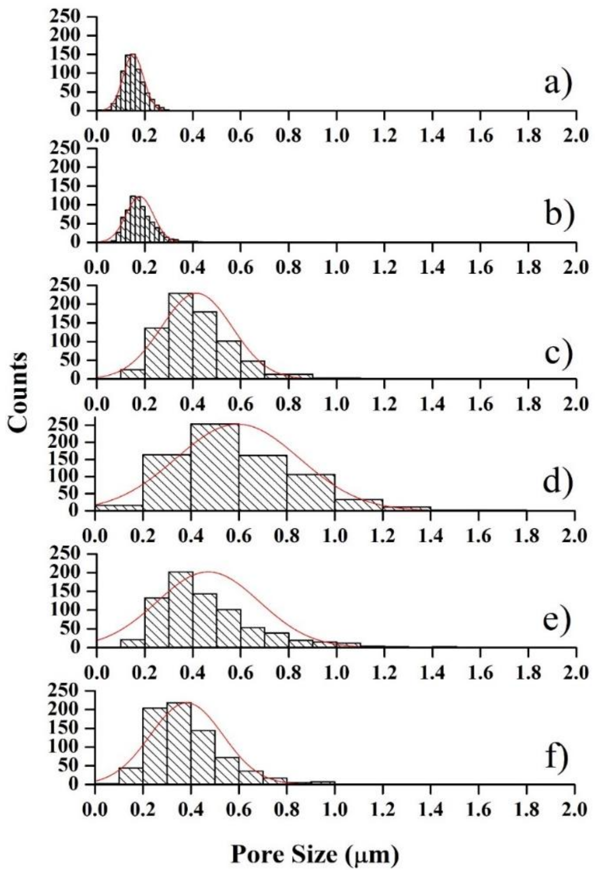

Figure 9. Pore size distribution of sintered r-CDT at different sintering temperature (a. 1425 ºC, b. 1500 ºC, c. 1575 ºC, d. 1650 ºC, e. 1725 ºC, f. 1800 ºC)

SEM and processed (by thresholding) images of the r-CDT sintered different temperatures are shown in Figure 10. When it is examined processed (by thresholding) images of the r-CDT sintered, it is observed that pores are interconnected at 1425 °C and 1500 °C (Figure 10 (b) and Figure 10 (d)). With increasing temperature pores are closed (isolated). Above 1650 °C, pores break into smaller pores. As can be seen on the Figure 8 (b), pore size decreases above 1650 °C. Therefore, processed images are consistent with Figure 8 (b).

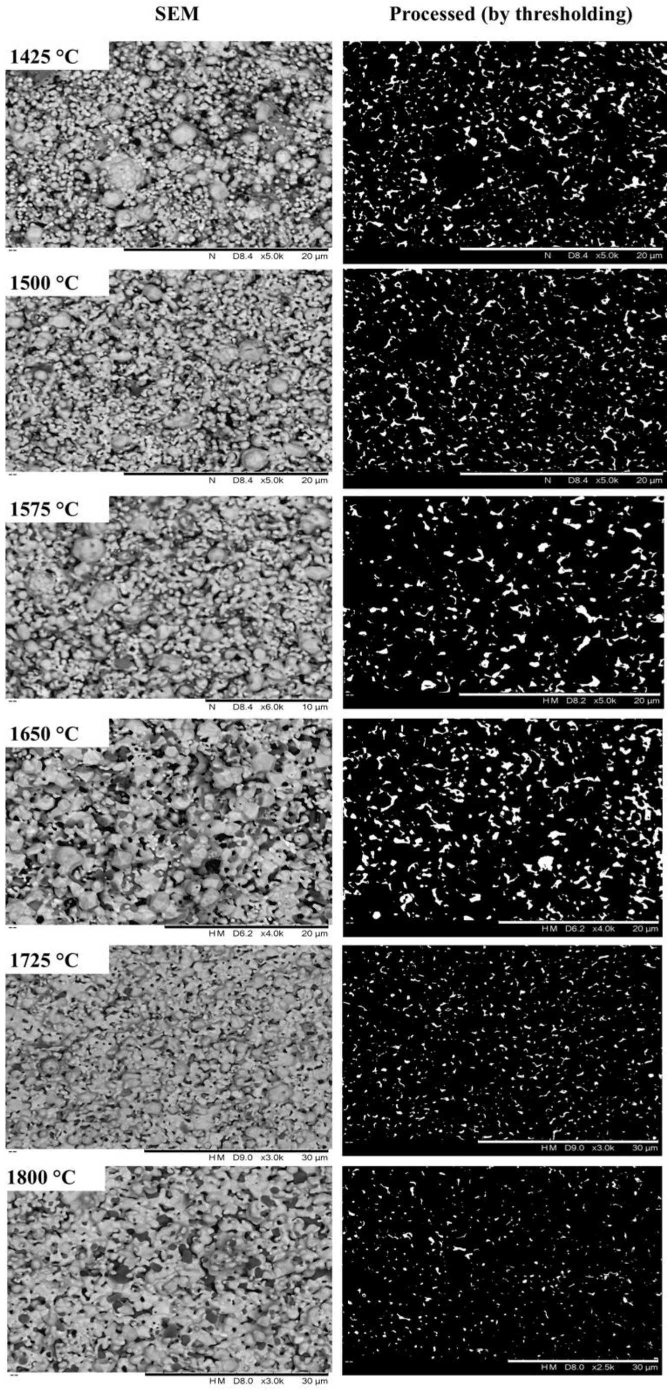

Figure 10. SEM and processed (by thresholding) images of the r-CDT sintered at different temperatures

The data collected from pellets are gathered and summarized in Table 1 as below.

Table 1. Pellet surface data after sintering

Sintering temperature (°C)	Pore size (µm)	Volume shrinkage (%)	Surface porosity (%)
1425	0.15	4.27	7.06
1500	0.18	4.1	7.1
1575	0.42	6.7	7.52
1650	0.6	11.34	10.91
1725	0.47	18.1	6.08
1800	0.38	28.77	3.9

The avererage pore size, volume shrinkage and surface porosity values are represented in Table 1. The average pore size and porosity are maximum at 1650 °C. However, volume shrinkage changed incrementally as the sintering temperature increases.

4. Mathematical Modelling

Sintering experiments were conducted at different temperatures. The sintered samples were examined with SEM and images were analysed by using ImageJ software. Average pore diameters were measured for each pellets individually. After gathering the experimental data set, pore diameter and sintering temperature relation was investigated via a mathematical modelling. This model represents two distinct regions as shown in Figure 11 and it is compatible with experimental results in Figure 8.

This model was constructed by using piece-wise functions. They are derived from the experiment-analysis data set fit functions. Equations are written in Equations 3-4:

Pore(T) =

$$\begin{cases} -1.06x10^{-7}T^3 + 0.00049T^2 - 0.774T + 398.62; \; 1425 \leq T \leq 1650°C & (3) \\ 95.91e^{-0.003T}; \quad 1650 \leq T \leq 1800°C & (4) \end{cases}$$

In the equation set, Pore(T) expresses the pore diameter in µm, and T defines the temperature in °C. The mathematical relation is constructed on two pieces of function. However, it can be distinguished that sintering temperature and pore size are linearly dependent in the initial phase. There is a slight transition to second order polynomial relation from initial to intermediate phase. As appeared in Figure 12, it is modelled with two separate functions. Initial and intermediate stages are expressed with one function. The pore diameters are still getting higher dimensions with increased temperatures. At the final phase, the pore diameter drastically decreases with increased sintering temperature. Therefore, this behaviour can be expressed with an exponential function which corresponds to 1650 – 1800 °C sintering temperature interval.

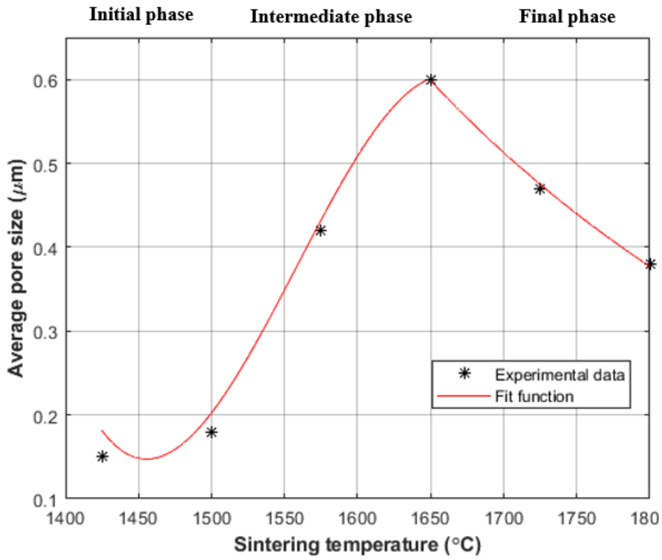

Figure 11. Sintering temperature and pore diameter relation

5. Conclusion

This study has demonstrated that sintering temperature plays a critical role in determining the microstructural and functional properties of r-CDT cathodes. The experimental results revealed that variations in sintering temperature directly influence the average pore size, surface porosity, and volume shrinkage of r-CDT pellets—all of which are key parameters affecting cathode emission performance, mechanical stability, and thermal behaviour. At lower sintering temperatures (1425–1500 °C), the structure retains high porosity with interconnected pores, favourable for emissive material transport but potentially limiting in terms of mechanical strength and thermal conductivity. As the sintering temperature increases (up to 1650 °C), pore size and porosity increase, reaching an optimum that balances material openness with improved structural coherence. Beyond 1650 °C, further increases in temperature lead to densification and a sharp reduction in both pore size and porosity due to pore closure and grain coalescence. This over-sintering effect may reduce emission efficiency by decreasing the available active surface area.

These findings confirm that the sintering temperature must be carefully controlled to tailor the r-CDT microstructure for desired operational conditions. The proposed mathematical model provides a valuable predictive tool for selecting the appropriate sintering parameters, allowing for efficient and cost-effective optimization of cathode fabrication. Ultimately, controlling the sintering behaviour enables the design of scandate cathodes with superior emission stability, structural durability, and performance reliability in advanced vacuum electronic devices.

Overall, understanding the relationship between pore size and sintering temperature in dispenser cathodes is essential for tailoring their properties to meet specific performance requirements. By controlling sintering parameters, manufacturers can engineer cathodes with superior emission efficiency, thermal stability, and mechanical durability, ensuring reliable performance in demanding applications such as satellite communications, microwave tubes, and high-power electron devices.

Declaration of Competing Interest

The authors declare that they have no known competing financial interests or personal relationships that could have appeared to influence the work reported in this paper.

Funding

This study was funded by TÜBİTAK BİLGEM.

Acknowledgement

This study was supported by TÜBİTAK BİLGEM Cathode and Microwave Vacuum Tube Research Center.

Authors' Contributions

Zeynep Hazal Yazğan: Investigation, Methodology, Data curation, Writing – original draft, Writing – review & editing, **Nergis Yıldız Angın Atmaca:** Investigation, Methodology, Data curation, Writing – original draft, Writing – review & editing, Project administration, **Okan Mert Yücedağ:** Investigation, Methodology, Data curation, Writing – original draft, Writing – review & editing, Project administration

References

[1] J. Xiu Bao, B. Fei Wan, *Appl. Surf. Sci*. (2006). https://doi.org/10.1016/j.apsusc.2005.08.012.

[2] I.P. Melnikova, V.G. Vorozheikin, D.A. Usanov, *Appl. Surf. Sci*. (2003). https://doi.org/10.1016/S0169-4332(03)00289-7.

[3] M.N. Seif, T.J. Balk, M.J. Beck, *Appl. Surf. Sci*. (2022). https://doi.org/10.1016/j.apsusc.2022.154541.

[4] M.N. Seif, Q. Zhou, X. Liu, T.J. Balk, M.J. Beck, *IEEE Trans. Electron Devices*. (2022). https://doi.org/10.1109/TED.2022.3172052.

[5] A. Shih, J.E. Yater, R. Abrams, *Appl. Surf. Sci*. (1999). https://doi.org/10.1016/S0169-4332(99)00062-8.

[6] G.L. Davis, *Powder Metall*. (1979). https://doi.org/10.1179/pom.1979.22.3.145.

[7] M. N. Seif, Q. Zhou, X. Liu, T. J. Balk ve M. J. Beck, (2022), https://doi.org/10.48550/arXiv.2202.04745

[8] F. Andreola, C. Leonelli, M. Romagnoli, *Am. Ceram. Soc. Bull*, 79 (2000).

[9] C. Selcuk, N. Morley, J. V. Wood, *Powder Metall*. (2005). https://doi.org/10.1179/003258905X37648.

[10] S. Nakagawa, "Impregnated cathode and method for manufacturing the same" (United States Patent Application Publication, 2001), https://patents.google.com/patent/US20010019239A1/en. Accessed 20 May 2023

[11] E.R. Kreidler, *J. Am. Ceram. Soc*. (1972). https://doi.org/10.1111/j.1151-2916.1972.tb13419.x.

[12] M. Wang, K. Hu, R. Wu, K. Khanlari, F. Zhang, B. Lin, *Adv. Powder Technol*. (2023). https://doi.org/10.1016/j.apt.2023.104133.

[13] Y. Cui, J. Wang, W. Liu, Y. Wang, M. Zhou, *Appl. Surf. Sci*. (2011). https://doi.org/10.1016/j.apsusc.2011.08.059.

[14] N. Shinohara, M. Okumiya, T. Hotta, K. Nakahira, M. Naito, K. Uematsu, *J. Am. Ceram. Soc.* (2000). https://doi.org/10.1111/j.1151-2916.2000.tb01442.x.

[15] R.M. German, *Sintering Theory and Practice*, (Wiley, New York, 1996), pp. 95-110.

[16] Z. Hu, K. Lu, *J. Am. Ceram. Soc.* (2014). https://doi.org/10.1111/jace.13080.

Bulletin of Materials Science & Metallurgy

Periodical Scientific Journal of UCTEA Chamber of Metallurgical and Materials Engineers

Volume 2, Issue 1, 2025, Pages 14-20 Received: 02 September 2025 Accepted: 13 October 2025

https://doi.org/10.70342/WSVX2145

Research Article

Aluminum Alloy with High Magnesium: Investigation of Melt Quality Refinement Methods and Resulting Properties

Kamil Armağan Gül[a,b,*], Eyüp Sabri Kayalı[a]

[a,]Istanbul Technical University, Istanbul,Turkiye

[b]Oyak-Renault Automobile Factories

*Corresponding author's email: rmagangul@gmail.com

Abstract

The industrial practice places a lot of emphasis on the development of lightweight, high-performance materials. When it comes to meet the requirement of volume production and to represent part complexities, Aluminum alloy production and casting are of great interest for their mechanical and lightweight properties. Alloy preparation step and obtain high quality melt for casting is crucial to obtaining the required mechanical and physical properties. Main challenge has been cleaning of the metal melt in order to obtain clean internal structure and resulting properties. Therefore, the most difficult task has been the production and melt treatment step of these alloys. In the present work, high magnesium content aluminum alloys have been fabricated by gravity sand casting method. As melt quality is the most important feature of a successful casting, melt cleanliness has been investigated by reduced pressure test and bifilm count has been measured as the increase in bifilm number has shown a significant decrease in mechanical performance. The performance of the alloys has been assessed by tensile tests. The proper scheme to achieve the highest melt quality has been identified by comparing different melt treatment methods. Moreover, traditional methods such as increased melt holding time and alloying of different elements have not shown an improvement in RPT assessments. On the other hand, rotary degasser method has been observed as ineffective for cleaning of the metal melt because of the turbulence created within the high Mg content. The optimum composition with the highest performance has been proposed.

Keywords

Casting, Aluminum, Mechanical Properties, Melt Quality, Reduced Pressure Test.

1. Introduction

Casting alloys have been widely used in industry since they are easy to manufacture at desired shapes. Different methods exist for the casting of different products [1]. Bifilm index studies and microstructural changes must be evaluated at the same time for aluminium alloys in order to assess the final properties of the alloy, since solely the microstructural investigation is not sufficient to obtain the required properties for aluminium alloys. Lack of joint evaluation of casting quality and microstructural evolution yielded variability of mechanical properties, which hinder extended usage of aluminium alloys in an application where mechanical performance and fatigue life is important [2-10].

During casting, it was shown by Campbell [11-12] that impurities and nonlinear flow of liquid create bifilms which are the defects causing failure of the components in service. The structure of the bifilms is multi-layered, closed, or semi-closed porosities that behave like a crack initiator in the part-in-service condition. In order to evaluate final properties, bifilm index measurements and pore formation must be studied and assessed for a given alloy system [13]. As the alloys tend to form bifilms and pores during solidification, there are also methods to improve melt cleanliness by several methods such as tablet addition to melt, purging gas through melt, degassing, shear methods, and runner design improvement [14-19]. Ultrasonic degassing methods have been investigated by Puga et al. [20–22], who proposed that three minutes of degassing is sufficient and optimal for cleaning the melt to increase mechanical properties. However, it is important to note that not all alloys and charges have the same quantity of bifilms or defects. Therefore, the duration of any degassing operation should not be limited to any period. It depends on the cleanliness level which could be controlled by bifilm index and then the casting decision can be made.

There has been debates that bifilms have been formed from external medium by the interaction of metal melt and ambient air. This approach has neglecting that intermetallic and bifilms which has been in the master or base alloys could be the main reason of the porosities and defects. In case of the different alloying elements, inherent bifilms must be removed to obtain a clean metal melt.

Some studies have also investigated the effectiveness of hold time of the melt at stable conditions as well as solidification rate impact on bifilm and porosity formation. The main purpose was to assess the effect of dissolved hydrogen within the melt and its effect on gas formation tendency. It has been shown that as the hold time increases, the pore formation increases [23]. Alloying elements are another important aspect in bifilm assessment. In literature, it has been shown for A356 alloys, Sr alloying yielded a lower bifilm index by leading to the formation of smaller and perfectly scattered bifilms [24]. Raiszadeh et al. [25] described this effect as a fusion of folded oxide bifilms and acts as a healing mechanism proposed by Campbell [1]. Effect of alloying elements on bifilm formation has been discussed by Gul et al [26] indicating that different alloying elements yielded different bifilm contents and incorporated variation in bifilm evolution.

The effectiveness of these methods is questionable and some of those methods have been discussed in the present work. In order to evaluate the melt cleanliness level, Dispinar [27–29] showed that molten aluminium melt quality must be identified which is most commonly possible and effective by Reduced pressure test (RPT). The evaluation of the metal solidification under vacuum gives a numerical count of pores linked to bifilm formation. The corresponding number is bifilm index giving an acceptable porosity range indication.

The Bifilm Index (BI) is a quantitative measure introduced to evaluate the amount of oxide film defects present in liquid metal. Calculation is based on reduced pressure test (RPT) results. Cross section of RPT specimens are analysed and size of the pores and quantities defines the BI according to equations 1.1 where h is the pore length of each pore observed in RPT sample cross section in mm and n is the number of pores.

$$BI = \sum_{i=1}^{n} h_i \qquad (1.1)$$

As the porosity and bifilm content can be measured, the quality index concept must be used to define the sufficient quality of the melt prior to casting. For this purpose, various quality index studies have been done by Caceres et al. [30–33]. Erzi et al. [34] proposed a new Supplier Quality Index approach to quantify and assess alloy melt quality using fluidity value, yield strength, tensile strength, elongation, and bifilm index value.

Melt quality and specimen quality have been assessed via Reduced pressure test (RPT)-solidification under vacuum. Bifilm counts have been done for RPT evaluations. Correlation with mechanical tests has been built.

Prior melt cleanliness work using RPT and the bifilm index (BI) has focused mainly on Al–Si–Mg casting by the following methods: pouring/runner design, and degassing methods, rotary degassing and shearing to enhance melt quality. Separate studies has outlined the hold time effects and oxide entrainment. Underexplored areas include high-Mg aluminium (>5 wt.% Mg) and Mg-rich Al–Mg–Cu melts where Mg's strong oxygen/hydrogen affinity governs bifilm formation and degassing efficiency.

Present study provides a comparison of the various melt treatment methods and their effect on melt quality of high containing Mg Al Alloys with side-by-side comparisons of treatment routes.

2. Experimental Methods

In the present study, three-steps of experimental procedure has been adopted. First, casting trials and design of experiments have been selected to manipulate the metal melt and affecting factors. Secondly, melt quality assessment procedures have been used to evaluate the effectiveness of the different methods and finally, mechanical testing procedures have been applied, and the results have been linked with melt quality assessment.

2.1. Casting Studies

AlMg5, A206, AlMg20 master alloys have been used as base in casting studies with main composition of Al-Mg and Al-Mg-Cu. Strontium, Boron and Titanium, Zirconium, Tin have been added in the form of master alloys to base alloy to evaluate the properties. The first set of Alloys have been numbered as Alloy A.n (n= 1-9) having alloying elements of Strontium, Boron and Titanium, Zirconium, Bismuth, Tin, Copper. Alternative of Alloy Ay has been selected with main alloying element of copper. Compositions are given in table 1.

Table 1. Main Constituents by wt.% for Alloy A.n and Ay

Alloy	Mg max	Cu		Sr max	Ti max	B max	Zr max	Sn max
A.n	5	*		400ppm	0,4	0,4	0,4	0,4
Ay	7	2		200ppm	0,4	0,4	0,4	*

Induction furnaces have been used for casting experiments. The melting temperature is set to 780ºC; during alloying it was lowered to 765ºC. The castings were done at 750ºC. Mammut A50 and A5 type crucibles have been used. 10 minutes of holding time have been selected. Sand mould castings have been done without any preheating.

Permanent steel moulds have been used in the experiments. In Figure 1, cupcake specimen geometry was given which was used for melt quality assessment experiments via RPT tests.

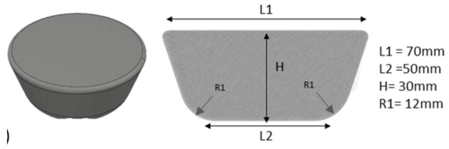

Figure 1. The geometry RPT Specimen

A5 crucibles have been used to identify the effect of different hold times for the same liquid level within the crucible at the same furnace condition with various holding times of 15, 30, and 45 minutes as shown in Figure 2.

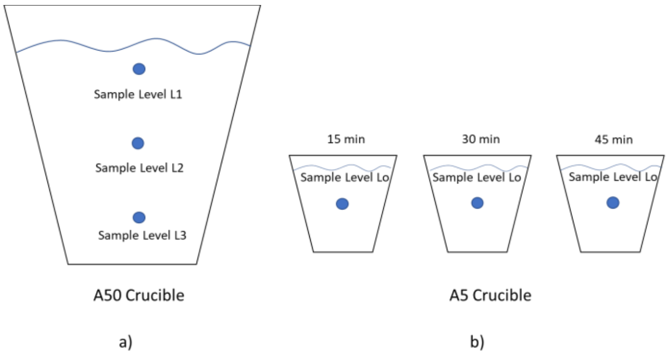

Figure 2. Effect of melt level and hold time effect: a) A50 Crucibles have been used to collect melt samples at different levels of the melt, b) A5 Crucibles have been used for holding time effect at the same level

A50 crucible has been used to assess the bifilm quantity and metal cleanliness on a large volume of metal melt. In this experimental setup, after a constant hold time of 30 minutes, consecutive castings have been done in order to sample alloy at different levels within the crucible.

Degassing method's effectiveness on the melt quality within a large volume of melt has been investigated. Rotary degassing and lance degassing methods have been applied to clean the metal melt using nitrogen gas. Rotary degassing parameters have been chosen as N_2 gas flow of 2 L/ min, rotation speed of 300 rpm for 10 minutes. Static lance degassing by immersion has been applied with N_2 gas flow of 2 L/ min into the molten metal for 10 min. Both degassers were immersed to the same metal level in the crucible.

2.2. Characterization Studies

In order to evaluate the bifilm level and melt cleanliness, reduced pressure tests were carried out at 100 mbar. Cross-section analysis of RPT specimens has been evaluated for different experiments of melt quality assessment. Image analysis was used to measure the pore size.

The mechanical property characterization has been done via tensile tests according to ASTM E8 standards. Specimen dimensions are as follows: head diameter, 8 mm; gauge diameter, 6 mm; gauge length, 30 ± 2 mm; R5 gauge radius. Tensile tests have been performed in stroke speed condition in Zwick tensile test machine at 1mm/ min head displacement. Hardness tests on the Brinell scale (2,5mm/1839N) have been done. The alloy's quality index has been calculated and evaluated according to Erzi et al [34].

3. Results and Discussion

3.1 Melt Quality and Bifilm Index Evolution

At the first stage of the casting studies, no degassing was carried out with an aim to evaluate the effect of bifilms on the properties.

In the second stage, the following methods of melt treatments have been respectively used: using selective alloying elements, molten metal level assessment, hold time increase, application of external vibration of the crucible, rotary degassing and lance degassing.

3.1.1 Alloying Element Effect

Effects of alloying elements into the Alloy A.n alloys on bifilm index change have been shown in Figure 3. Alloying elements drastically change bifilm index. However, none of the alloying elements could provide melt quality increase therefore a degassing method must be applied. All additions have increased the oxide content. All these values appeared to be in the 'bad quality' classification which was defined by Dispinar [29].

Increasing the melt cleanliness by Bi and Sn addition was applied if Bi could create a stable oxide layer on the top of the melt metal and Sn to protect Mg content within the melt thus preventing oxidation of the metal. On this context, Alloy A.8 has been cast but the method yielded ineffective results due to compositional deviations. Alloy A9 has been cast and results has been presented in rotary degassing section.

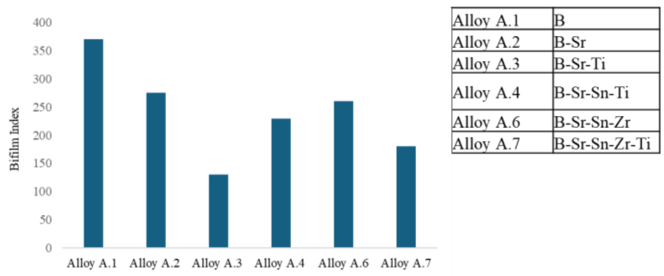

Figure 3. Bifilm index of Al-Mg Alloys by alloying[26]

3.1.2 Melt Level and Hold Time Effect

Figure 4 shows the effect of metal melt level on bifilm formations on Alloy A.7. Although the surface of the melt has been skimmed off, the bifilms are ascending within the metal melt towards the top of the crucible. The decrease in bifilm content can be seen from the cross-sections.

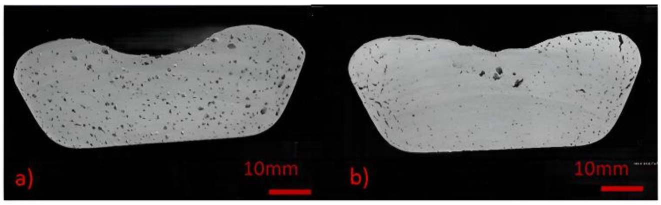

Figure 4. Alloy A7 bifilm index change at (a) Level 1 and (b) Level 3 (according to Figure 2a)

Bifilm formation and RPT cross-sections of 15- and 45-minutes holding time of different but identical composition crucibles have been shown in Figure 5. As the holding time had increased, the pore size has not changed significantly however the number of pores increased slightly. This is mainly attributed to neutral buoyancy and interaction of the bifilms-aluminum matrix during the process.

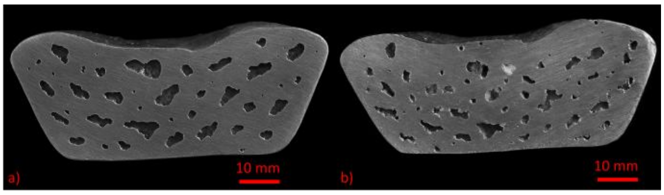

Figure 5. Alloy A7 bifilm change at holding times of (a) 15minutes and (b) 45 minutes.

3.1.3 Rotary and Lance Degassing Methods

As for Figure 6, the effect of rotary degasser has been shown for Alloy A9 whose composition contains B-Ti-Sr-Zr with %5 Mg. The rotary degasser provides improvement in bifilm index. Nevertheless, alloy melt quality is far from the good quality level.

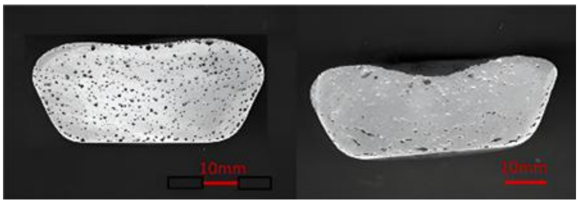

(a) b)

Figure 6. Effect of Rotary Degasser (a) Before Degassing (b) After Degassing

On the last approach, lance degassing was carried out in the melt with ceramic diffusor. The assumption is the airflow outward lance tip should push the oxides to the surface This situation was schematically shown as a balloon/feather analogy by Yorulmaz [35].

During the casting stage, 5 minutes of degassing was applied after the alloying was done for Alloy AY1. Afterward, 5 minutes of holding time, reduced pressure test sample collected. Figure 7 shows the effect of melt quality impact of lance degasser. Static immersed lance degassing process has proven its effectiveness as per literature [35-36].

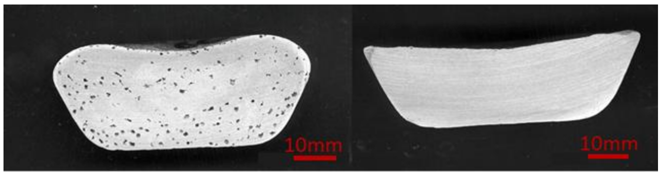

Figure 7. Effect of Lance Degasser Alloy AY1 a) before degassing, b) after degassing

3.1.3 Buoyancy Modification by External Excitation

In order to overcome the neutral buoyancy problem, the A5 crucible has been vibrated externally during hold time regime but it has no positive effect on the metal quality. Therefore, the results are not presented in detail.

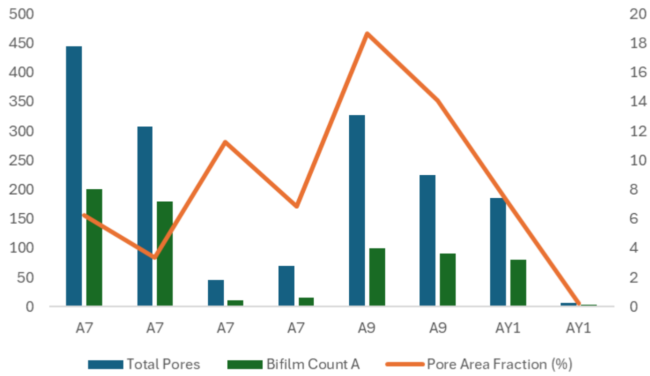

Figure 8. Pore Quantity and Bifilm Calculation Results

Figure 8 provides pore quantities, area fraction and bifilm counts of the specimen cross sections that were presented in figure 4-7.

3.4 Hardness Results of Al-Mg Alloys

Table 3 summarizes hardness profiles of Set A and Set B to assess bifilm effects of hardness. Hardness evolution in Set A in Figure 9, gives the variation of hardness at the same metal melt level, with 30 minutes and 15 minutes hold time respectively according to figure3b of Alloy A7.

Set B gives the effect of hold time within the crucible as per figure 3a at level2 and level3 of Alloy A7. As Bifilm level increases hardness decreased.

As per Set A results, it is clearly obvious that increasing the hold time does not increase the melt quality, furthermore, this decreases the mechanical properties. On the other hand, as per Set B, the fact that the crucible has a different section of metal melt each having different melt qualities affects the properties as well.

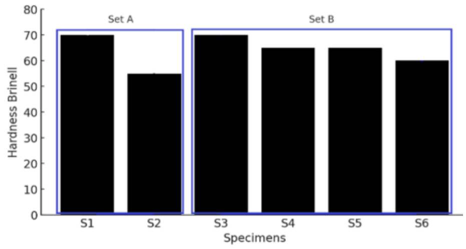

Figure 9. Effect of Hold Time and Melt Level to the Hardness of Alloy A7

3.5 Tensile Test Results of Degassed Specimens

In the final step, degassed specimens A.9 and AY have been tested, and results has been presented in Table 5.

Table 4. Mechanical Properties of as-cast Al-Mg alloy specimens. (Sand Mould Casting)

Degassing Type	Alloy	Tensile Strength MPa	% Elongation	Bifilm Index
Lance	AY	157	1	x<50
Lance	AY	168	0.65	x<50
Rotary	A.9	133	0.55	x~100
Rotary	A.9	127	0.47	x>100

As degassing overcame the non-degassing methods, tensile test results have been given for degassed specimens on Al-Mg and Al-Mg-Cu Alloy of Y series.

4. Discussion

Although alloying proposes an improvement in properties, the present study has shown that metal melt quality is negatively influenced by each additional alloying therefore proper melt treatment is mandatory.

Selective alloying of elements has not shown any improvement if degassing has not applied. This has been attributed to the intermetallic formation with neutral buoyancy. Moreover, the affinity of magnesium to create oxides and affinity to hydrogen could not be prevented by any alloying elements.

As proposed by Gyarmati [6] the use of flux during degassing operations was more efficient in cleaning the melt than the sole use of rotary degasser . In the present study, flux addition has not been discussed and the effect on high magnesium alloys have not been investigated.

Hold time or crucible external vibration has been found ineffective because as per figure 5 and figure 8 bifilm index has not been improved with above mentioned methods. BI results were 45 and 69 in hold time experiments and similar trends has been encountered in crucible external vibration.

Inducing vibration onto the crucible has been found ineffective because the methodology has failed to exert any internal excitation to the bifilms and to separate them from the melt.

Different melt levels in large crucible have shown variable bifilm indexes due to stable melt movement in the crucible. Therefore, bifilms and other melt defects varied along different horizontal volume sections of the melt. Similar findings were reported by Ghanaatian [38].

Rotary degasser (RD) has been found ineffective which has been attributed to large inert gas bubbles and insufficient shear force applied by the rotor blades in high magnesium containing Al alloys.

Lance degassing has proven the most effective method to clean the metal melt of high Mg-Aluminium alloys. This has been attributed to static lance with multiple small gas bubbles which have swept defects toward to the surface of the metal melt.

5. Conclusion

Effect of alloying elements on the mechanical property improvement of any alloy must be coupled with proper melt quality cleanliness in order to achieve high mechanical properties.

The effect of Bi and Sn in metal melt quality has been found to have no effect. Therefore, alloying of Bi and Sn are not viable options for metal quality enhancement.

Flux application should be investigated in future studies. Rotary degassing parameters should be optimized (depth, rotation speed) in future studies

Authors' Contributions

Conceptualization: Kamil Armağan Gül, Methodology: Eyüp Sabri Kayalı, Investigation: Kamil Armağan Gül, Validation: Kamil Armağan Gül, Resources: Eyüp Sabri Kayalı, Data curation: Kamil Armağan Gül, Eyüp Sabri Kayalı, Writing—original draft preparation: Kamil Armağan Gül, Writing—review and editing: Kamil Armağan Gül, Eyüp Sabri Kayalı, Supervision: Eyüp Sabri Kayalı

Declaration of Competing Interest

The authors declare that they have no known competing financial interests or personal relationships that could have appeared to influence the work reported in this paper.

Acknowledgement:

Armagan Gul would like to thank Dr. Derya Dispinar for his support of the casting studies.

References

1. J. Campbell, Complete casting handbook: metal casting processes, metallurgy, techniques and design. Butterworth-Heinemann, 2015.
2. M. Tiryakioğlu, J. Campbell, and N. D. Alexopoulos, "On the ductility of cast Al-7 pct Si-Mg alloys," Metall. Mater. Trans. A, vol. 40, no. 4, p. 1000, 2009.
3. A. Ardekhani and R. Raiszadeh, "Removal of double oxide film defects by ceramic foam filters," J. Mater. Eng. Perform., vol. 21, no. 7, pp. 1352–1362, 2012.
4. J. Mi, R. A. Harding, and J. Campbell, "Effects of the entrained surface film on the reliability of castings," Metall. Mater. Trans. A, vol. 35, no. 9, pp. 2893–2902, 2004.
5. G. Gyarmati, G. Fegyverneki, T. Mende, and M. Tokár, "Characterization of the double oxide film content of liquid aluminum alloys by computed tomography," Mater. Charact., vol. 157, p. 109925, 2019.
6. G. Gyarmati, G. Fegyverneki, M. Tokár, and T. Mende, "The Effects of Rotary Degassing Treatments on the Melt Quality of an Al–Si Casting Alloy," Int. J. Met., pp. 1–11, 2020.
7. G. Lasko, M. Apel, A. Carré, U. Weber, and S. Schmauder, "Effect of Microstructure and Hydrogen Pores on the Mechanical Behavior of an Al7% Si0. 3% Mg Alloy Studied by a Combined Phase-Field and Micromechanical Approach," Adv. Eng. Mater., vol. 14, no. 4, pp. 236–247, 2012.
8. H. Song et al., "Three-dimensional reconstruction of bifilm defects," Scr. Mater., vol. 191, pp. 179–184, 2021.
9. M. Mostafaei, M. Ghobadi, G. Eisaabadi, M. Uludağ, and M. Tiryakioğlu, "Evaluation of the effects of rotary degassing process variables on the quality of A357 aluminum alloy castings," Metall. Mater. Trans. B, vol. 47, no. 6, pp. 3469–3475, 2016.
10. C. Do Lee, "Variability in the impact properties of A356 aluminum alloy on microporosity variation," Mater. Sci. Eng. A, vol. 565, pp. 187–195, 2013.
11. J. Campbell, "Entrainment defects," Mater. Sci. Technol., vol. 22, no. 2, pp. 127–145, 2006.
12. J. Campbell, "Stop pouring, start casting," Int. J. Met., vol. 6, no. 3, pp. 7–18, 2012.
13. D. Dispinar and J. Campbell, "Reduced pressure test (RPT) for bifilm assessment," in Shape Casting: 5th International Symposium 2014, 2014, pp. 243–251.
14. G. E. Bozchaloei, N. Varahram, P. Davami, and S. K. Kim, "Effect of oxide bifilms on the mechanical properties of cast Al–7Si–0.3 Mg alloy and the roll of runner height after filter on their formation," Mater. Sci. Eng. A, vol. 548, pp. 99–105, 2012.
15. M. Uludağ, R. Çetin, D. Dispinar, and M. Tiryakioğlu, "Characterization of the Effect of Melt Treatments on Melt Quality in Al-7wt %Si-Mg Alloys," Metals (Basel)., 2017.
16. D. Eskin, N. Alba-Baena, T. Pabel, and M. da Silva, "Ultrasonic degassing of aluminium alloys: basic studies and practical implementation," Mater. Sci. Technol., vol. 31, no. 1, pp. 79–84, 2015.
17. Z. Y. Fan, Y. B. Zuo, and B. Jiang, "A new technology for treating liquid metals with intensive melt shearing," in Materials Science Forum, 2011, vol. 690, pp. 141–144.
18. Y. B. Zuo, B. Jiang, Y. J. Zhang, and Z. Fan, "Degassing LM25 aluminium alloy by novel degassing technology with intensive melt shearing," Int. J. Cast Met. Res., vol. 26, no. 1, pp. 16–21, 2013.
19. T. Yamamoto, K. Kato, S. V Komarov, Y. Ueno, M. Hayashi, and Y. Ishiwata, "Investigation of melt stirring in aluminum melting furnace through Water model," J. Mater. Process. Technol., vol. 259, pp. 409–415, 2018.
20. H. Puga, J. Barbosa, T. Azevedo, S. Ribeiro, and J. L. Alves, "Low pressure sand casting of ultrasonically degassed AlSi7Mg0. 3 alloy: modelling and experimental validation of mould filling," Mater. Des., vol. 94, pp. 384–391, 2016.
21. H. Puga, J. Barbosa, J. C. Teixeira, and M. Prokic, "A new approach to ultrasonic degassing to improve the mechanical properties of aluminum alloys," J. Mater. Eng. Perform., vol. 23, no. 10, pp. 3736–3744, 2014.
22. H. Puga, J. Barbosa, E. Seabra, S. Ribeiro, and M. Prokic, "The influence of processing parameters on the ultrasonic degassing of molten AlSi9Cu3 aluminium alloy," Mater. Lett., vol. 63, no. 9–10, pp. 806–808, 2009.
23. M. Uludağ, L. Gemi, R. Çetin, and D. Dispinar, "The effect of holding time and solidification rate on porosity of A356," Am. J. Eng. Res., vol. 5, no. 12, pp. 271–275, 2016.
24. B. Atakav, Ö. Gürsoy, E. Erzi, K. Tur, and D. Dispinar, "Sr addition and its effect on the melt cleanliness of A356," Mater. Res. Express, vol. 7, no. 2, p. 26549, 2020.
25. R. Raiszadeh and W. D. Griffiths, "The effect of holding liquid aluminum alloys on oxide film content," Metall. Mater. Trans. B, vol. 42, no. 1, pp. 133–143, 2011.
26. Gul, A., Gürsoy, Ö., Erzi, E., Dispinar, D., Kayali, E. (2019). Aluminum Alloy with High Mg Content: Casting Studies for Microstructural Evolution, Phase Formation and Thermophysical Properties with Different Alloying Elements. In: Tiryakioğlu, M., Griffiths, W., Jolly, M. (eds) Shape Casting. The Minerals, Metals & Materials Series. Springer, Cham. https://doi.org/10.1007/978-3-030-06034-3_33
27. D. Dispinar and J. Campbell, "Critical assessment of reduced pressure test. Part 1: Porosity phenomena," Int. J. Cast Met. Res., vol. 17, no. 5, pp. 280–286, 2004.
28. D. Dispinar and J. Campbell, "Critical assessment of reduced pressure test. Part 2: Quantification," Int. J. Cast Met. Res., vol. 17, no. 5, pp. 287–294, 2004.
29. D. Dispinar and J. Campbell, "Use of bifilm index as an assessment of liquid metal quality," Int. J. Cast Met. Res., vol. 19, no. 1, pp. 5–17, 2006.
30. C. H. Cáceres, "A phenomenological approach to the Quality Index of Al-Si-Mg casting alloys," Int. J. Cast Met. Res., vol. 12, no. 6, pp. 367–375, 2000.
31. C. H. Cáceres, "A rationale for the quality index of Al-Si-Mg casting alloys," Int. J. Cast Met. Res., vol. 12, no. 6, pp. 385–391, 2000.
32. C. H. Cáceres, "Microstructure design and heat treatment selection for casting alloys using the quality index," J. Mater. Eng. Perform., vol. 9, no. 2, pp. 215–221, 2000.
33. C. H. Cáceres and J. Barresi, "Selection of temper and Mg content to optimise the quality index of Al-7Si-Mg casting

alloys," Int. J. Cast Met. Res., vol. 12, no. 6, pp. 377–384, 2000.
34. E. Erzi, Ö. Gürsoy, Ç. Yüksel, M. Colak, and D. Dispinar, "Determination of Acceptable Quality Limit for Casting of A356 Aluminium Alloy: Supplier's Quality Index (SQI)," Metals (Basel)., vol. 9, no. 9, p. 957, 2019.
35. A. Yorulmaz, E. Erzi, O. Gursoy, and D. Dispinar, "End product rejection rate and its correlation with melt treatment in direct-chill casted hot rolling slabs," Int. J. Cast Met. Res., vol. 32, no. 3, pp. 164–170, 2019.
36. Gul, A., Dispinar, D. & Aslan, O. Effect of Ti–V and Nb addition on the properties of AlMg7Cu1.2 Alloy. *Inter Metalcast* (2025). https://doi.org/10.1007/s40962-024-01545-9
37. Gul, K.A., Dispinar, D., Kayali, E.S. *et al*. Assessment of Tensile Properties of Cast High Mg containing Al-Mg-Cu Aluminum Alloy with Correlation of Computed Tomography Scans and Optical Crack Surface Analysis. *Inter Metalcast* **17**, 2622–2637 (2023). https://doi.org/10.1007/s40962-023-01038-1
38. Ghanaatian, MH., Raiszadeh, R. "Effect of Different Methods for Removing Bifilm Defects from A356 Aluminum Alloy". Metall Mater Trans B (2022).

BMSM
Bulletin of Materials Science & Metallurgy

Periodical Scientific Journal of UCTEA Chamber of Metallurgical and Materials Engineers

Volume 2, Issue 1, 2025, Pages 21-27 Received: 17 September 25 Accepted: 30 October 2025

https://doi.org/10.70342/WFFG7935

Research Article

Optimisation of Machining Fixture Design for Milling Operation of Ductile Iron Coach Suspension Arm Component

Mustafa Burak Terzioğlu*, Bülent Şirin, İsmail Şile

DÖKTAŞ Dökümcülük Ticaret ve Sanayi A.Ş.

*Corresponding author's email: mustafaburak.terzioglu@doktas.com

Abstract

Within the scope of this study, the machining fixture design and optimization studies of a bus rear suspension arm made of spheroidal cast iron were carried out using CAD (computer aided design) and CAE (computer aided engineering) programs. The suspension arm is the safety part that turns the bus rear suspension more comfortable, to which the air bellows, shock absorbers and axle are connected. The machining fixture plays an important role in the machinability of the part. The fixture of the suspension arm part was shaped using topology optimization. The fixture design, which was created and subjected to a DFM (Design for Manufacturability) study, was finalized through structural analysis, taking into account the cutting and clamping forces. The cutting and clamping forces used in the structural analyses were calculated empirically, and the resulting values were optimized using DOE (Design of Experiments) methods. As a result, a fixture design based on engineering-oriented topology optimization was successfully developed in this study. The resulting fixture was found to be approximately 42,45% lighter than those designed using conventional methods, yet it exhibited higher rigidity. Structural analyses confirmed that the fixture provided sufficient resistance to the cutting and clamping forces encountered during machining. Dimensional measurements conducted after the machining process demonstrated that the workpiece met the technical drawing tolerances. In this respect, the optimized fixture design offers an effective solution that enhances both manufacturing accuracy and structural efficiency.

Keywords

Machining Fixture Design, Topology Optimization, Spheroidal Cast Iron, Finite Element Analysis (FEA), Vibration and Rigidity

1. Introduction

In contemporary industrial applications, casting methods continue to hold significant importance in the manufacturing of components with complex geometries and high structural strength. Among these, spheroidal graphite cast irons (EN-GJS grade) are widely preferred in the automotive and heavy vehicle sectors due to their superior properties of ductility, strength, and machinability. In this material class, the transformation of graphite morphology from lamellar to spheroidal form markedly enhances the mechanical properties. To achieve this spheroidization, rare earth elements such as cerium (Ce) and magnesium (Mg) are added to the molten iron bath, resulting in a microstructure that simultaneously provides ductility and strength [1]. Owing to these attributes, spheroidal graphite cast irons play a critical role in applications requiring load-bearing capacity, vibration resistance, and long service life. In this study, the machining fixture design and optimization of a rear suspension arm of a bus, manufactured from EN-GJS-500-7 spheroidal graphite cast iron, were carried out to ensure suitability for milling operations. The suspension arm, serving as the component to which air bellows, shock absorbers, and axle elements are attached, directly affects comfort and safety in the rear suspension system of the vehicle. Due to its complex surface geometry, limited clamping regions, and exposure to high cutting loads, the safe and accurate machining of such parts in CNC machining centres is only possible through the implementation of a properly designed fixture [2]. Fixture design not only ensures the positioning and clamping of the workpiece but also guarantees rigidity against cutting and clamping forces during machining, which necessitates optimization according to engineering criteria. In this context, during the initial phase of the study, a fixture system suitable for machining the component was modelled in Siemens NX CAD environment using conventional methods. Special attention was given to the regions subject to surface milling operations, clamping and supporting points were defined accordingly. With indicated x1, x2, x3 points as shown in figure 1, datum plane created for locating the part on fixture. After that, with y1, y2 and z1 points alignment has been ensured.

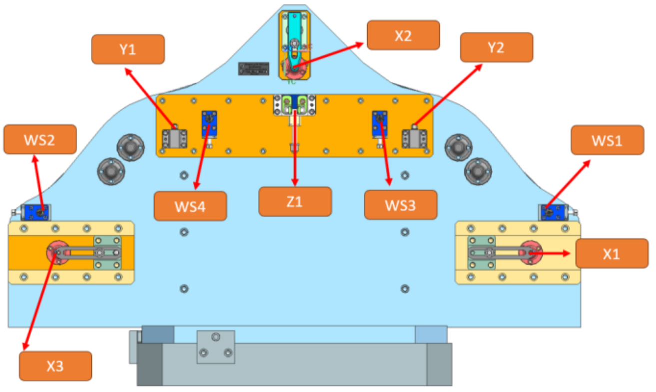

Figure 1. Fixture design in a 3D CAD environment

Subsequently, cutting forces generated during machining were calculated empirically, and their effects on the fixture supports were evaluated through structural analysis using Altair OptiStruct software. The analyses identified deformation and vibration-prone regions of the workpiece, which were reinforced by integrating support elements (work supports), thereby establishing a more rigid clamping system. Following the validation of the fixture design, topology optimization was applied to the same model with the aim of reducing mass while maintaining structural integrity. As a result of optimization studies conducted in the OptiStruct platform, the initial fixture mass of 1,477 kg was reduced by approximately 42,45%, resulting in a final weight of 850 kg. This improvement not only provided significant weight reduction but also enhanced performance. According to structural analysis results, the maximum displacement, which was 88 microns in the initial model, decreased to 68 microns in the topology-optimized fixture, indicating higher rigidity despite the lower weight. In conclusion, a comprehensive fixture design process was conducted within this thesis by integrating CAD and CAE tools with engineering-based parameters. The developed methodology produced a fixture design that is both manufacturable and structurally optimized, enabling reliable clamping that minimizes deformation and vibration-induced quality issues during milling operations. This study contributes to the literature by presenting a systematic methodology applicable to low-rigidity and geometrically complex workpieces, combining manufacturability principles with advanced structural optimization to achieve an efficient and reliable fixture design.

2. Materials and Methods

2.1. Materials

2.1.1. Material of Machining Part (Coach Suspension Arm)

Spheroidal graphite cast iron is a type of cast iron enriched in carbon, in which the graphite structures are present in a nodular form. Owing to its spheroidal (nodular) graphite particles in the microstructure, this material provides superior properties such as high ductility, impact resistance, and strength [1]. This material is defined by a minimum tensile strength of 500 MPa and a minimum elongation of 7%. The Microstructure of EN-GJS-500-7 captured by optical microscope has shown in figure 2.

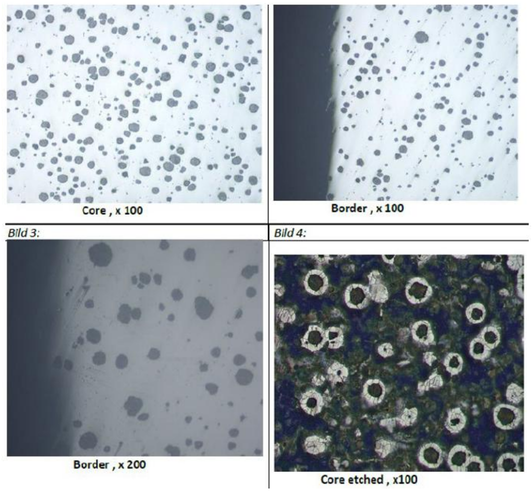

Figure 2. Microstructure of EN-GJS-500-7

2.1.2. Material of Base Plate and Rear Plate

The body elements used in fixture design (the base plate and the rear plate) are the fundamental structures that provide the overall rigidity of the fixture and directly interface with the machine table. Since these components both support the self-weight of the fixture and absorb the loads generated by cutting tools and clamping forces, the selected material must be evaluated in terms of its mechanical properties, weldability, machinability, and cost. For cases where the plates must be welded prior to machining, ST 52-3 provides significant advantages. It can be easily joined using MIG/MAG welding methods without preheating and exhibits low susceptibility to embrittlement in the heat-affected zone [3]. In this study, the fixture bodies were manufactured by plasma cutting, surface finishing, and welding of ST 52-3 plates, with the rear plate being 65 mm thick and the base plate 50 mm thick. This configuration provided durability against cutting forces during milling operations while also offering a rigid mounting surface to the machine table.

2.1.3. Material of Machining Fixture Components

In the machining fixture developed within the scope of this thesis, the blocks containing fixed locators and clamping mechanisms were manufactured from AISI 4140 alloy steel in order to meet both high mechanical strength and machinability requirements. This steel belongs to the group of quenched and tempered steels and is widely used in industry due to its suitability for heat treatment as well as its versatile engineering properties. AISI 4140 is a chromium-molybdenum alloy steel, equivalent to 42CrMo4 in the DIN standard. Its chemical composition typically includes 0.38–0.43% carbon, 0.75–1.0% chromium, 0.15–0.25% molybdenum, and 0.8–1.1% manganese [4]. The combination of these alloying elements provides the material with high tensile strength, hardenability, toughness, and wear resistance. These attributes are particularly critical for fixture elements directly subjected to mechanical loads, such as clamping and guiding during machining operations. Furthermore, tempering reduces brittleness and enhances impact resistance, ensuring reliable performance against sudden loads, impact forces, or vibrations occurring during workpiece placement [5]. In fixtures, fixed locators are employed to accurately determine the position of the workpiece and to prevent positional shifts during machining.

2.2. Method

2.2.1. Fixture Design in CAD Environment

Initially, the fixture design was modelled using Siemens NX CAD software based on the 3-2-1 locating principle. Considering the complex geometry of the workpiece and the force distribution during machining, the fixture was meticulously designed with clearly defined fixed locators, clamping points, and support regions. Fixture locating and alignment points have to be defined for every machined parts. This phenomenon calls as 3-2-1 principle which shown in figure 3.

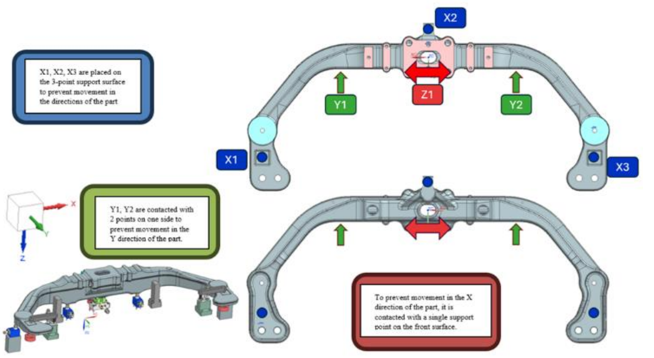

Figure 3. Representation of 3-2-1 principle.

2.2.2. Displacement and Modal Analysis

The finite element method (FEM) is a computational technique used in engineering to obtain approximate solutions of boundary value problems. A boundary value problem is defined as a mathematical problem in which one or more dependent variables must satisfy a differential equation throughout a known domain of independent variables while also fulfilling specified conditions at the boundaries of the domain The fundamental characteristics of finite elements are embedded in the stiffness matrix. For a structural finite element, the stiffness matrix contains the information on geometric and material behaviour that demonstrates the resistance of an element subjected to loads against deformation Figure 4 illustrates a spring element.

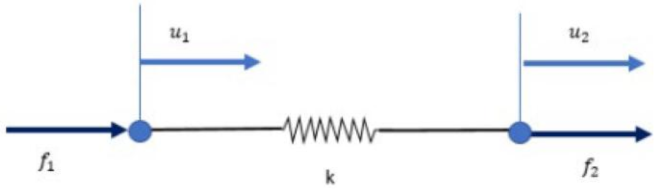

Figure 4. Spring system schematic [6].

In the analysis of systems using FEM, bodies that are in reality composed of infinitely many points are discretized into a finite number of elements. These elements contain different numbers of nodes depending on their type. Calculations are carried out through these nodal points. Essentially, there are three types of elements: one-dimensional, two-dimensional, and three-dimensional [7]. Within these categories, the number of edges, surfaces, and nodal points varies depending on the element type. The choice of element type for a component is determined by considering the geometrical characteristics of the component. A significant number of studies in fixture design have focused on improving machining performance by reducing the adverse effects of deformation, vibration, and stress on the workpiece. The existing literature provides valuable insights into fixture design principles, optimization techniques, and analytical methods for evaluating fixture performance. In this study, finite element analysis (FEA) was conducted to evaluate the deformation and stresses induced on the workpiece under the effect of cutting forces during machining. The workpiece and fixture components were modelled in a CAD environment and integrated into the analysis software. Material properties were defined under the assumption of linear elasticity, while boundary conditions were determined by considering the forces arising during machining. Taking into account the cutting parameters, the load acting on the workpiece was calculated as 5261 N. Under these conditions, the finite element modelling studies were carried out using Altair HyperMesh. Tetrahedral elements were employed in the meshing stage. During the face milling operation, the tool load was applied in the +Z direction at four points on the workpiece surface, corresponding to the regions where the cutting insert was expected to exert the maximum effect. The vector of applied cutting forces for milling operation has been realized as indicated in figure 5.

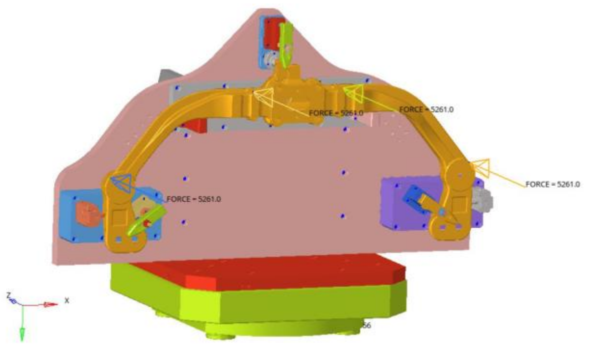

Figure 5. Representation of forces applied during the face milling process.

Modal analysis, also referred to as frequency analysis, is employed to determine the natural frequencies of a structure and the corresponding mode shapes. Vibration modes define how a structure vibrates in the absence of damping and external excitation forces. Although every real structure inherently possesses infinitely many degrees of freedom, it nevertheless exhibits a finite number of discrete vibration modes. Each mode is associated with a specific frequency and a corresponding mode shape, representing the state in which the stiffness forces of the structure are balanced by the inertial forces. In this study, the modal analysis of the fixture and workpiece assembly was performed in Altair OptiStruct using the EIGRL method. The structure was modelled as mounted from the machine-tool interface region, and its operational condition was examined.

2.2.3. Topology Optimization

Optimization is the act, process, or method of making something (such as a design, system, or decision) as flawless, functional, or effective as possible [6]. Topology optimization, on the other hand, involves determining the ideal material distribution within a design. A key factor contributing to the increasing preference for topology optimization methods among designers in recent years is that the optimal structure can be identified at the early stages of the design process. Two commonly used approaches in topology optimization studies are the homogenization method and the material distribution method [8,9]. The definitions related to topology optimization were implemented in Altair HyperMesh. The solver employed was Altair OptiStruct, the first commercial structural optimization code. The optimization process was carried out iteratively, and the final result was obtained after 36 iterations. The optimization outcome is presented as follows. In the legend, points representing values close to 1 indicate regions where material should be retained in the design, whereas elements with values close to 0 were automatically removed using Altair HyperView post-processing software, thereby revealing the ideal material distribution. The outputs of topology optimization analyses at Altair HyperView represented in figure 6.

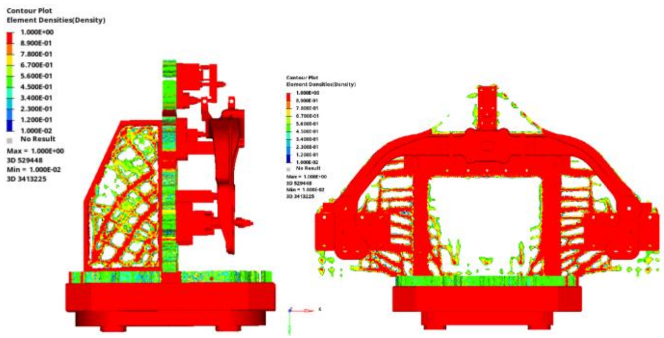

Figure 6. Results of topology optimization

2.2.4. Design for manufacturing

In this study, the fixture geometry outputs obtained through topology optimization were primarily analysed in terms of sheet metal processing, plasma cutting, and 3-axis CNC machining methods. The curvilinear and organic structures resulting from the optimization are, in many cases, too complex to be directly manufactured using conventional subtractive manufacturing techniques [10]. Therefore, planar surfaces and 2.5D features were preserved, particularly in load-bearing plates and support elements, to facilitate cutting, machinability, and ease of clamping. From a DFM (Design for Manufacturability) perspective, these modifications simplified each component to allow manufacturing with a minimum number of machining operations. For instance, instead of curvilinear internal cavities, triangular or rectangular openings were used, which both facilitated material removal and simplified tool path planning. Additionally, regions requiring welding during assembly were replaced with bolted connections, enhancing both disassemblability and maintainability. This approach not only reduced manufacturing time but also minimized operator errors.

2.2.5. Determination of cutting and clamping forces

The cutting forces applied to the workpiece were calculated using empirical formulas, based on the cutting parameters of a Ø160 mm face milling tool and the EN-GJS-500-7 material. The clamping forces were determined based on the maximum forces applicable by the mechanical clamping systems used to secure the workpiece.

3. Results and Discussion

In this study, a machining fixture for a bus rear suspension arm component, manufactured from spheroidal graphite cast iron (EN-GJS-500-7), was designed using Siemens NX CAD (Computer-Aided Design) in accordance with conventional 3-2-1 clamping principles. Fixed support and clamping points were established, and subsequently, milling operations with a Ø160 face mill—including both roughing and finishing passes—were simulated along with the clamping forces on the fixture using Altair OptiStruct CAE (Computer-Aided Engineering) software. Cutting forces generated during material removal were applied over regions corresponding to the cutter edge size, and both modal and structural analyses were performed. The initial design exhibited a displacement of 262 μm, indicating that structural interventions were required in vibration-prone regions of the system. Accordingly, the thickness of the rear plate was increased and mechanical support elements were integrated at the ends of the workpiece. These improvements led to Version 2 of the design, where the displacement was reduced to 82 μm, which was established as the system acceptance criterion which shown in figure 7.

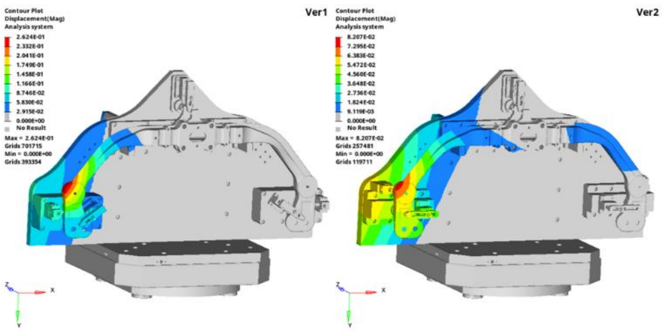

Figure 7. Displacement result comparison of version1 and version2 designs.

Based on this criterion, topology optimization was applied to Version 2, with the objective of reducing the remaining volume of the fixture plates by 50% which it's called as Version 3 in the experiment. The topology optimization outputs were examined, incorporated into the 3D model, and the updated design was subjected to further modal and structural analyses. Also, there were two additional studies have been carried out till the final result at version 6. In the version 4, in order to increase the system rigidity and decrease the displacement values, triangular shaped support plates have been designed and located to the appropriate locations is shown in figure 8. After the finite element analyses for version 4, the displacement values have been decreased to 168 μm and modal frequency has been decreased to 111 Hz.

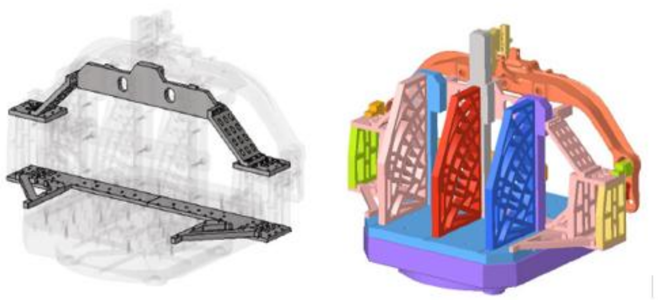

Figure 8. Additional supports on Version 4

At version 5, support plates that shown in figure 9 which have been designed at version 4, have been linked each other with supports to reduce the vibration at construction. With this method, displacement values have been decreased to 92 μm.

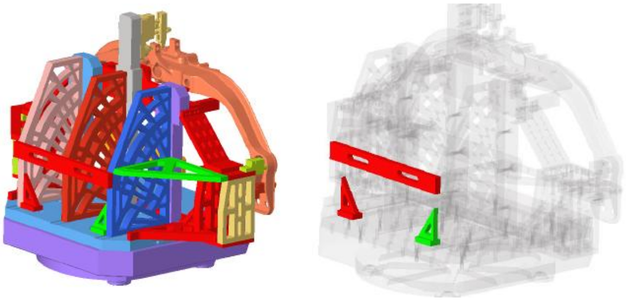

Figure 9. Additional supports on Version 5

Design revisions have been finalised when the displacement was reduced under 82 μm which is the acceptance criteria for the version 2. The final design (version 6) achieved a displacement of 67 μm, and the first natural frequency remained well above the spindle frequency range of the machining center, confirming that the system posed no resonance risk. Consequently, Version 2 was determined to provide excellent rigidity, ensuring surface quality and tool life. In addition to improvements in structural strength and first mode frequency, the topology-optimized design, referred to as Version 6, reduced the fixture weight from 1477 kg to 850 kg. This weight reduction not only decreases manufacturing costs but also enhances the machining accuracy and dynamic stability of dual-pallet CNC machining centres, thereby providing industrial benefits and contributing to the national economy. The version 2 fixture model, obtained from structural analyses, was subjected to topology optimization with a target volume reduction of 50%. During this process, a minimum wall thickness of 20 mm and a maximum of 50 mm were set as constraints, considering manufacturability via plasma cutting. The topology optimization results, generated using Altair Inspire software, were interpreted from an engineering perspective to develop versions 3, 4, 5, and finally version 6 of the design. Each new version underwent modal and strength analyses again, maintaining an iterative improvement cycle. The fixture has been simulated for 4 different machining areas and the results has been presented in Figure 10.

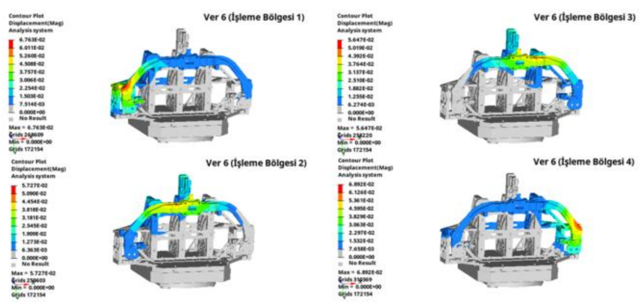

Figure 10. Version6 results of four machining areas

3.1. Weight and Material Consumption

As a result of topology optimization, the fixture weight was measured as 1477 kg in Version 2 and 850 kg in the Version 6 design. This corresponds to an approximate 42,45% reduction in weight. This weight reduction not only provided ergonomic advantages but also had a direct positive impact on the dynamic performance of CNC machines.

Using a lighter fixture, especially in dual-pallet CNC machines, eliminated load imbalance, resulting in increased machining precision. Additionally, the reduced weight helped prevent wear on spindle bearings, aiming to extend the machine's service life.

3.2. Modal Analysis Characterization

When comparing modal analysis results for different versions, the first mode frequency was measured as 82 Hz for Version 2 and 118 Hz for Version 6. The higher natural frequency indicates that the system is more resistant to external vibration sources and poses no resonance risk. This condition positively affects cutting tool life and surface quality, particularly during long-duration machining operations.

3.3. Modal Analysis Characterization

Rigidity, one of the most critical criteria in fixture design, was enhanced with each version. According to the finite element analyses conducted:

- Version 2 fixture: 82 Hz first mode frequency, 82 µm maximum displacement
- Version 6 fixture: 118 Hz first mode frequency, 67 µm maximum displacement

This difference revealed a significant increase in dynamic rigidity between the versions. Additionally, this increase was confirmed to have a direct positive effect on the workpiece surface quality through surface roughness measurements.

3.4. Mass Reduction and Manufacturing Ease

As a result of topology optimization, a mass reduction of up to 42,45% in the fixture weight was achieved, positively impacting the CNC machine performance:

- Version 2 weight: 1477 kg
- Version 6 weight: 850 kg

This weight reduction not only saved material and lowered production costs but also improved the machining balance of the CNC machine. Especially, the pallet imbalance problem occurring in dual-pallet systems was largely eliminated.

3.5. Modular Structure

The modular approach adopted in the design has made this fixture usable for different parts as well. Components that can be assembled and disassembled like Lego pieces have been made reusable for parts of different sizes with minimal modifications. Thus, there was no need for a separate fixture investment for each part, providing flexibility in the production process. This flexibility demonstrates that the fixture design offers not only a technical but also an economical solution. In order to present as image, render has been created at NX CAD which indicated as figure 11.

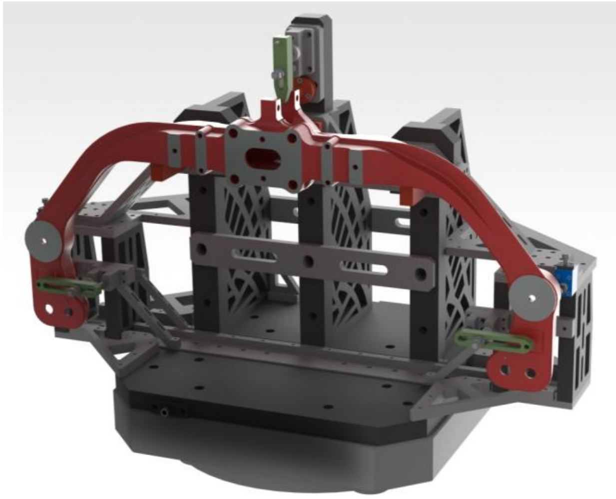

Figure 11. Render images of the final fixture design

3.6. Manufacturing Accuracy and Quality

Measurements taken with the CMM showed that all dimensions of the suspension arm machined with the Version 6 fixture remained within the technical drawing tolerance ranges. This indicates that the fixture was able to prevent surface deformations and enabled first-time-right manufacturing. Additionally, vibration marks on the part after production were significantly reduced compared to the non-optimized fixture, and the cutting tool life increased. This also reveals the fixture’s potential to reduce maintenance and tooling costs in the long term.

4. Conclusion

In this study, the fixture structure required for machining a bus rear suspension arm made of ductile cast iron was designed, analysed, and improved using CAD/CAE-based numerical methods and topology optimization. Moving beyond traditional design approaches, loads based on empirical calculations were modelled with finite element methods, the behaviour under these loads was observed, and rigidity was increased.

As a result of the design improvements and optimization efforts:

- Fixture rigidity was increased by 18%,
- Mass was reduced by 42,45%,
- Vibrations and deformations occurring during machining were minimized.

Additionally, thanks to its modular structure, the fixture was made adaptable to workpieces of different sizes, providing manufacturing flexibility. This enabled both a reduction in per-part costs and increased efficiency in CNC machines.

The developed fixture fully complied with technical drawing tolerances and contributed to the principle of "first-time-right" manufacturing. Improvements observed in surface quality, cutting tool life, and machining time demonstrate the industrial applicability and sustainability of the proposed method.

Authors' Contributions

Conceptualization: Mustafa Burak Terzioğlu, Methodology: Mustafa Burak Terzioğlu, Bülent Şirin, İsmail Şile, Investigation: Mustafa Burak Terzioğlu, Bülent Şirin, İsmail Şile, Validation: Mustafa Burak Terzioğlu, Bülent Şirin, İsmail Şile, Formal Analysis: Mustafa Burak Terzioğlu, Resources: Bülent Şirin, İsmail Şile, Mustafa Burak Terzioğlu, Data Curation: Mustafa Burak Terzioğlu, Writing—Original Draft Preparation: Mustafa Burak Terzioğlu, Writing—Review and Editing: Mustafa Burak Terzioğlu, Bülent Şirin, İsmail Şile, Supervision: Bülent Şirin, Project Administration: Mustafa Burak Terzioğlu

Declaration of Competing Interest

The authors declare that they have no known competing financial interests or personal relationships that could have appeared to influence the work reported in this paper.

Acknowledgement

We would like to thank Döktaş Dökümcülük R&D department for their support.

References

[1] Çetin, A. (2016), Küresel Grafitli Dökme Demir, Ankara, El Kitabı Dökümhane Eğitim Projesi Özel Sayı Serisi.

[2] Hodgson, A., Chen, X., (2008), A Methodology for The Development of Machining Fixtures for Components with Complicated Geometry,International Journal of Computer Integrated Manufacturing.

[3] ŞIK, Aydın. (2007). A Research into the Effect of Additional Electrode Types and Protective Mixture Gases on the Bending Fatigue Life of Steel Material That is Welded with MIG/MAG Welding Method, Gazi University Journal of Science.

[4] Tecer, M.M. (2020) Effects of Various Heat Treatment Procedures on the Toughness of AISI 4140 Low Alloy Steel. The Internal Journal of Materials and Engineering Technology 003,131-149.

[5] Çoban, O. (2025) Heat Treatment of AISI 1040 and AISI 4140 Steels: Microstructure-Mechanical Property Relationships for Normalization, Spheroidization and Quenching-Tempering. Journal of Innovative Engineering and Natural Science.

[6] Hutton, D.V. (2004) Fundamental of Finite Element Analysis. McGraw Hill Companies, New York.

[7] Martins, J.A., Kövesdy, I., (2012), Overview in the Application of FEM in Mining and the Study of Case: Stress Analysis in Pulleys of Stacker-Reclaimers: FEM vs. Analytical, Applications in Mechanical Engineering. InTech.

[8]- Bendsøe, O.S., (1999), Material interpolation schemes in topology optimization, Archive of Applied Mechanics 69, 635-654 .

[9]- Bendsøe, M.P., Kikuchi N., (1988), Genarating Optimal Topologies in Structural Design Using a Homogenization Method, Computer Methods in Applied Mechanics and Engineering 71, 197-224, North Holland.

[10]- Kerbrat, O., Mognol, P., Hascoet, J-Y., (2011), A New DFM Approach to Combine Machining and Additive Manufacturing, Institut de Recherche en Communications et Cybernetique de Nantes.